

Hemodynamic Deconvolution Demystified: Sparsity-Driven Regularization at Work

Eneko Uruñuela^{a,b,*}, Thomas A.W. Bolton^{c,d}, Dimitri Van De Ville^{c,e}, César Caballero-Gaudes^{a,*}

^a*Basque Center on Cognition, Brain and Language (BCBL), Donostia-San Sebastián, Spain.*

^b*University of the Basque Country (EHU/UPV), Donostia-San Sebastián, Spain.*

^c*Ecole Polytechnique Fédérale de Lausanne (EPFL), Lausanne, Switzerland.*

^d*Gamma Knife Center, Department of Clinical Neuroscience, Centre Hospitalier Universitaire Vaudois (CHUV), Lausanne, Switzerland*

^e*Faculty of Medicine, University of Geneva, Geneva, Switzerland*

Abstract

Deconvolution of the hemodynamic response is an important step to access short timescales of brain activity recorded by functional magnetic resonance imaging (fMRI). Albeit conventional deconvolution algorithms have been around for a long time (e.g., Wiener deconvolution), recent state-of-the-art methods based on sparsity-pursuing regularization are attracting increasing interest to investigate brain dynamics and connectivity with fMRI. This technical note revisits the main concepts underlying two main methods, Paradigm Free Mapping and Total Activation, in the most accessible way. Despite their apparent differences in the formulation, these methods are theoretically equivalent as they represent the synthesis and analysis sides of the same problem, respectively. We demonstrate this equivalence in practice with their best-available implementations using both simulations, with different signal-to-noise ratios, and experimental fMRI data acquired during a motor task and resting-state. We evaluate the parameter settings that lead to equivalent results, and showcase the potential of these algorithms compared to other common approaches. This note is useful for practitioners interested in gaining a better understanding of state-of-the-art hemodynamic deconvolution, and aims to answer questions that practitioners often have regarding the differences between the two methods.

Keywords: fMRI deconvolution, paradigm free mapping, total activation, temporal regularization

1. Introduction

Functional magnetic resonance imaging (fMRI) data analysis is often directed to identify and disentangle the neural processes that occur in different brain regions during task or at rest. As the blood oxygenation level-dependent (BOLD) signal of fMRI is only a proxy for neuronal activity mediated through neurovascular coupling, an intermediate step that estimates the activity-inducing signal, at the timescale of fMRI, from the BOLD timeseries can be useful. Conventional analysis of task fMRI data relies on the general linear models (GLM) to establish statistical parametric maps of brain activity by regression of the empirical timecourses against hypothetical ones built from

*Corresponding authors

Email addresses: e.urunuela@bcbl.eu (Eneko Uruñuela), c.caballero@bcbl.eu (César Caballero-Gaudes)

9 the knowledge of the experimental paradigm. However, timing information of the paradigm can be
10 unknown, inaccurate, or insufficient in some scenarios such as naturalistic stimuli, resting-state, or
11 clinically-relevant assessments.

12 Deconvolution and methods alike are aiming to estimate neuronal activity by undoing the
13 blurring effect of the hemodynamic response, characterized as a hemodynamic response function
14 (HRF)¹. Given the inherently ill-posed nature of hemodynamic deconvolution, due to the strong
15 temporal low-pass characteristics of the HRF, the key is to introduce additional constraints in the
16 estimation problem that are typically expressed as regularizers. For instance, the so-called Wiener
17 deconvolution is expressing a “minimal energy” constraint on the deconvolved signal, and has
18 been used in the framework of psychophysiological interaction analysis to compute the interaction
19 between a seed’s activity-inducing timecourse and an experimental modulation (5–9). Complementarily,
20 the interest in deconvolution has increased to explore time-varying activity in resting-state
21 fMRI data (10–13). In that case, the aim is to gain better insights of the neural signals that drive
22 functional connectivity at short time scales, as well as learning about the spatio-temporal structure
23 of functional components that dynamically construct resting-state networks and their interactions
24 (14).

25 Deconvolution of the resting-state fMRI signal has illustrated the significance of transient, sparse
26 spontaneous events (15, 16) that refine the hierarchical clusterization of functional networks (17)
27 and reveal their temporal overlap based on their signal innovations not only in the human brain (18),
28 but also in the spinal cord (19). Similar to task-related studies, deconvolution allows to investigate
29 modulatory interactions within and between resting-state functional networks (20, 21). In addition,
30 decoding of the deconvolved spontaneous events allows to decipher the flow of spontaneous thoughts
31 and actions across different cognitive and sensory domains while at rest (18, 22, 23). Beyond findings
32 on healthy subjects, deconvolution techniques have also proven its utility in clinical conditions
33 to characterize functional alterations of patients with a progressive stage of multiple sclerosis at
34 rest (24), to find functional signatures of prodromal psychotic symptoms and anxiety at rest on
35 patients suffering from schizophrenia (25), to detect the foci of interictal events in epilepsy patients
36 without an EEG recording (26, 27), or to study functional dissociations observed during non-rapid
37 eye movement sleep that are associated with reduced consolidation of information and impaired
38 consciousness (28).

39 The algorithms for hemodynamic deconvolution can be classified based on the assumed hemo-
40 dynamic model and the optimization problem used to estimate the neuronal-related signal. Most
41 approaches assume a linear time-invariant model for the hemodynamic response that is inverted
42 by means of variational (regularized) least squares estimators (5, 6, 17, 29–36), logistic functions
43 (37–39), probabilistic mixture models (40), convolutional autoencoders (41) or nonparametric homomor-
44 phic filtering (42). Alternatively, several methods have also been proposed to invert non-linear
45 models of the neuronal and hemodynamic coupling (43–49).

46 Among the variety of approaches, those based on regularized least squares estimators have been
47 employed more often due to their appropriate performance at small spatial scales (e.g., voxelwise).
48 Relevant for this work, two different formulations can be established for the regularized least-
49 squares deconvolution problem, either based on a synthesis- or analysis-based model (50, 51). The
50 rationale of the synthesis-based model is that we know or suspect that the true signal (here, the

¹Note that the term deconvolution is also alternatively employed to refer to the estimation of the hemodynamic response shape assuming a known activity-inducing signal or neuronal activity (1–4).

51 neuronally-driven BOLD component of the fMRI signal) can be represented as a linear combination
 52 of predefined patterns or dictionary atoms (for instance, the hemodynamic response function). In
 53 contrast, the analysis-based approach considers that the true signal is analyzed by some relevant
 54 operator and the resulting signal is small (i.e., sparse).

55 As members of the groups that developed Paradigm Free Mapping (synthesis-based solved with
 56 regularized least-squares estimators such as ridge-regression (**author?**) 29 or LASSO (**author?**)
 57 31) and Total Activation (analysis-based also solved with a regularized least-squares estimator using
 58 generalized total variation (**author?**) 17, 52) deconvolution methods for fMRI data analysis,
 59 we are often contacted by researchers who want to know about the similarities and differences be-
 60 tween the two methods and which one is better. *It depends*—and to clarify this point, this note
 61 revisits synthesis- and analysis-based deconvolution methods for fMRI data and comprises four sec-
 62 tions. First, we present the theory behind these two deconvolution approaches based on regularized
 63 least squares estimators that promote sparsity: Paradigm Free Mapping (PFM) (31) — available
 64 in AFNI as *3dPFM*² and *3dMEPFM*³ for single-echo and multi-echo data, respectively — and
 65 Total Activation (TA) (17) — available as part of the *iCAPs toolbox*⁴. We describe the similar-
 66 ties and differences in their analytical formulations, and how they can be related to each other.
 67 Next, we assess their performance controlling for a fair comparison on simulated and experimental
 68 data. Finally, we discuss their benefits and shortcomings and conclude with our vision on potential
 69 extensions and developments.

70 2. Theory

71 2.1. Notations and definitions

72 Matrices of size N rows and M columns are denoted by boldface capital letters, e.g., $\mathbf{X} \in \mathbb{R}^{N \times M}$,
 73 whereas column vectors of length N are denoted as boldface lowercase letters, e.g., $\mathbf{x} \in \mathbb{R}^N$. Scalars
 74 are denoted by lowercase letters, e.g., k . Continuous functions are denoted by brackets, e.g., $h(t)$,
 75 while discrete functions are denoted by square brackets, e.g., $x[k]$. The Euclidean norm of a matrix
 76 \mathbf{X} is denoted as $\|\mathbf{X}\|_2$, the ℓ_1 -norm is denoted by $\|\mathbf{X}\|_1$ and the Frobenius norm is denoted by
 77 $\|\mathbf{X}\|_F$. The discrete integration (**L**) and difference (**D**) operators are defined as:

$$\mathbf{L} = \begin{bmatrix} 1 & 0 & \dots & & \\ 1 & 1 & 0 & \dots & \\ 1 & 1 & 1 & 0 & \dots \\ \vdots & \ddots & \ddots & \ddots & \ddots \end{bmatrix}, \quad \mathbf{D} = \begin{bmatrix} 1 & 0 & \dots & & \\ 1 & -1 & 0 & \dots & \\ 0 & \ddots & \ddots & \ddots & \dots \\ \vdots & \ddots & 0 & 1 & -1 \end{bmatrix}.$$

78 2.2. Conventional general linear model analysis

Conventional general linear model (GLM) analysis puts forward a number of regressors incor-
 porating the knowledge about the paradigm or behavior. For instance, the timing of epochs for

²https://afni.nimh.nih.gov/pub/dist/doc/program_help/3dPFM.html

³https://afni.nimh.nih.gov/pub/dist/doc/program_help/3dMEPFM.html

⁴<https://c4science.ch/source/iCAPs/>

a certain condition can be modeled as an indicator function $p(t)$ (e.g., Dirac functions for event-related designs or box-car functions for block-designs) convolved with the hemodynamic response function (HRF) $h(t)$, and sampled at TR resolution (53–56):

$$x(t) = p * h(t) \rightarrow x[k] = p * h(k \cdot \text{TR}).$$

The vector $\mathbf{x} = [x[k]]_{k=1,\dots,N} \in \mathbb{R}^N$ then constitutes the regressor modelling the hypothetical response, and several of them can be stacked as columns of the design matrix $\mathbf{X} = [\mathbf{x}_1 \dots \mathbf{x}_L] \in \mathbb{R}^{N \times L}$, leading to the well-known GLM formulation:

$$\mathbf{y} = \mathbf{X}\boldsymbol{\beta} + \mathbf{e}, \quad (1)$$

where the empirical timecourse $\mathbf{y} \in \mathbb{R}^N$ is explained by a linear combination of the regressors in \mathbf{X} weighted by the parameters in $\boldsymbol{\beta} \in \mathbb{R}^L$ and corrupted by additive noise $\mathbf{e} \in \mathbb{R}^N$. Under independent and identically distributed Gaussian assumptions of the latter, the maximum likelihood estimate of the parameter weights reverts to the ordinary least-squares estimator; i.e., minimizing the residual sum of squares between the fitted model and measurements. The number of regressors L is typically much less than the number of measurements N , and thus the regression problem is over-determined and does not require additional constraints or assumptions (57).

In the deconvolution approach, no prior knowledge of the hypothetical response is taken into account, and the purpose is to estimate the deconvolved activity-inducing signal \mathbf{s} from the measurements \mathbf{y} , which can be formulated as the signal model

$$\mathbf{y} = \mathbf{H}\mathbf{s} + \mathbf{e}, \quad (2)$$

where $\mathbf{H} \in \mathbb{R}^{N \times N}$ is a Toeplitz matrix that represents the discrete convolution with the HRF, and $\mathbf{s} \in \mathbb{R}^N$ is a length- N vector with the unknown activity-inducing signal. Note that the temporal resolution of the activity-inducing signal and the corresponding Toeplitz matrix is generally assumed to be equal to the TR of the acquisition, but it could also be higher if an upsampled estimate is desired. Despite the apparent similarity with the GLM equation, there are two important differences. First, the multiplication with the design matrix of the GLM is an expansion as a weighted linear combination of its columns, while the multiplication with the HRF matrix represents a convolution operator. Second, determining \mathbf{s} is an ill-posed problem given the nature of the HRF. As it can be seen intuitively, the convolution matrix \mathbf{H} is highly collinear (i.e., its columns are highly correlated) due to large overlap between shifted HRFs (see Figure 2C), thus introducing uncertainty in the estimates of \mathbf{s} when noise is present. Consequently, additional assumptions under the form of regularization terms (or priors) in the estimate are needed to reduce their variance. In the least squares sense, the optimization problem to solve is given by

$$\hat{\mathbf{s}} = \arg \min_{\mathbf{s}} \frac{1}{2} \|\mathbf{y} - \mathbf{H}\mathbf{s}\|_2^2 + \Omega(\mathbf{s}). \quad (3)$$

The first term quantifies data fitness, which can be justified as the log-likelihood term derived from Gaussian noise assumptions, while the second term $\Omega(\mathbf{s})$ brings in regularization and can be interpreted as a prior on the activity-inducing signal. For example, the ℓ_2 -norm of \mathbf{s} (i.e., $\Omega(\mathbf{s}) = \lambda \|\mathbf{s}\|_2^2$) is imposed for ridge regression or Wiener deconvolution, which introduces a trade-off between the data fit term and “energy” of the estimates that is controlled by the regularization parameter λ . regularized terms are related to the elastic net (i.e., $\Omega(\mathbf{x}) = \lambda_1 \|\mathbf{x}\|_2^2 + \lambda_2 \|\mathbf{x}\|_1$) [REF].

92 *2.3. Paradigm Free Mapping*

In paradigm free mapping (PFM), the formulation of Eq. (3) was considered equivalently as fitting the measurements using the atoms of the HRF dictionary (i.e., columns of \mathbf{H}) with corresponding weights (entries of \mathbf{s}). This model corresponds to a synthesis formulation. In (author?) 31 a sparsity-pursuing regularization term was introduced on \mathbf{s} , which in a strict way reverts to choosing $\Omega(\mathbf{s}) = \lambda\|\mathbf{s}\|_0$ as the regularization term and solving the optimization problem (58). However, finding the optimal solution to the problem demands an exhaustive search across all possible combinations of the columns of \mathbf{H} . Hence, a pragmatic solution is to solve the convex-relaxed optimization problem for the l_1 -norm, commonly known as Basis Pursuit Denoising (59) or equivalently as the least absolute shrinkage and selection operator (LASSO) (60):

$$\hat{\mathbf{s}} = \arg \min_{\mathbf{s}} \frac{1}{2} \|\mathbf{y} - \mathbf{H}\mathbf{s}\|_2^2 + \lambda\|\mathbf{s}\|_1, \quad (4)$$

93 which provides fast convergence to a global solution. Imposing sparsity on the activity-inducing
94 signal implies that it is assumed to be well represented by a reduced subset of few non-zero coeffi-
95 cients at the fMRI timescale, which in turn trigger event-related BOLD responses. Hereinafter, we
96 refer to this assumption as the *spike model*. However, even if PFM was developed as a spike model,
97 its formulation in Eq.(4) can be extended to estimate the innovation signal, i.e., the derivative of
98 the activity-inducing signal, as shown in section 2.5.

99 *2.4. Total Activation*

Alternatively, deconvolution can be formulated as if the signal to be recovered directly fits the measurements and at the same time satisfies some suitable regularization, which leads to

$$\hat{\mathbf{x}} = \arg \min_{\mathbf{x}} \frac{1}{2} \|\mathbf{y} - \mathbf{x}\|_2^2 + \Omega(\mathbf{x}). \quad (5)$$

100 Under this analysis formulation, total variation (TV), i.e., the l_1 -norm of the derivative $\Omega(\mathbf{x}) =$
101 $\lambda\|\mathbf{Dx}\|_1$, is a powerful regularizer since it favors recovery of piecewise-constant signals (61). Going
102 beyond, the approach of generalized TV introduces an additional differential operator $\mathbf{D}_\mathbf{H}$ in the
103 regularizer that can be tailored as the inverse operator of a linear system (52), that is, $\Omega(\mathbf{x}) =$
104 $\lambda\|\mathbf{DD}_\mathbf{H}\mathbf{x}\|_1$. In the context of hemodynamic deconvolution, Total Activation is proposed for which
105 the discrete operator $\mathbf{D}_\mathbf{H}$ is derived from the inverse of the continuous-domain linearized Balloon-
106 Windkessel model (62, 63). The interested reader is referred to (17, 52, 64) for a detailed description
107 of this derivation.

Therefore, the solution of the Total Activation (TA) problem

$$\hat{\mathbf{x}} = \arg \min_{\mathbf{x}} \frac{1}{2} \|\mathbf{y} - \mathbf{x}\|_2^2 + \lambda\|\mathbf{DD}_\mathbf{H}\mathbf{x}\|_1 \quad (6)$$

108 will yield the activity-related signal \mathbf{x} for which the activity-inducing signal $\mathbf{s} = \mathbf{D}_\mathbf{H}\mathbf{x}$ and the
109 so-called innovation signal $\mathbf{u} = \mathbf{Ds}$, i.e., the derivate of the activity-inducing signal, will also be
110 available, as they are required for the regularization. We refer to modeling the activity-inducing
111 signal based on the innovation signal as the *block model*. Nevertheless, even if TA was originally
112 developed as a block model, its formulation in Eq.(6) can be made equivalent to the spike model
113 as shown in section 2.5.

114 *2.5. Unifying both perspectives*

115 PFM and TA are based on the synthesis- and analysis-based formulation of the deconvolution
116 problem, respectively. They are also tailored for the spike and block model, respectively. In the first
117 case, the recovered deconvolved signal is synthesized to be matched to the measurements, while in
118 the second case, the recovered signal is directly matched to the measurements but needs to satisfy
119 its analysis in terms of deconvolution. This also corresponds to using the forward or backward
120 model of the hemodynamic system, respectively. Hence, it is possible to make both approaches
121 equivalent (50)⁵.

122 To start with, TA can be made equivalent to PFM by adapting it for the spike model; i.e., when
123 removing the derivative operator \mathbf{D} of the regularizer in Eq. (6), it can be readily verified that
124 replacing in that case $\mathbf{x} = \mathbf{H}\mathbf{s}$ leads to identical equations and thus both assume a spike model,
125 since \mathbf{H} and $\mathbf{D}_\mathbf{H}$ will cancel out each other (52)⁶.

Conversely, the PFM spike model can also accommodate the TA block model by modifying Eq.
(4) with the forward model $\mathbf{y} = \mathbf{H}\mathbf{L}\mathbf{u} + \mathbf{e}$. Here, the activity-inducing signal \mathbf{s} is rewritten in terms
of the innovation signal \mathbf{u} as $\mathbf{s} = \mathbf{L}\mathbf{u}$ where the matrix \mathbf{L} is the first-order integration operator
(34, 65). This way, PFM can estimate the innovation signal \mathbf{u} as follows:

$$\hat{\mathbf{u}} = \arg \min_{\mathbf{u}} \frac{1}{2} \|\mathbf{y} - \mathbf{H}\mathbf{L}\mathbf{u}\|_2^2 + \lambda \|\mathbf{u}\|_1, \quad (7)$$

126 and becomes equivalent to TA by replacing $\mathbf{u} = \mathbf{DD}_\mathbf{H}\mathbf{x}$, and thus adopting the block model. Based
127 on the previous equations (4), (6) and (7), it is clear that both PFM and TA can operate under the
128 spike and block models, providing a convenient signal model according to the different assumptions
129 of the underlying neuronal-related signal. This work evaluates the core of the two techniques; i.e.,
130 the regularized least-squares problem with temporal regularization without considering the spatial
131 regularization term originally incorporated in TA. For the remainder of this paper, we will use the
132 PFM and TA formalisms with both spike and block models.

133 *2.6. Algorithms and parameter selection*

134 Despite their apparent resemblance, the practical implementations of the PFM and TA methods
135 proposed different algorithms to solve the corresponding optimization problem and select an
136 adequate regularization parameter λ (17, 31). The PFM implementation available in AFNI em-
137 ploys the least angle regression (LARS) (66), whereas the TA implementation uses the fast iterative
138 shrinkage-thresholding algorithm (FISTA) (67). The blue box in Figure 1 provides a descriptive
139 view of the iterative *modus operandi* of the two algorithms.

140 On the one hand, LARS is a homotopy approach that computes all the possible solutions to
141 the optimization problem and their corresponding value of λ ; i.e., the regularization path, and the
142 solution according to the Bayesian Information Criterion (BIC) (68), was recommended as the most
143 appropriate in the case of PFM approaches since AIC often tends to overfit the signal(31, 32).

On the other hand, FISTA is an extension of the classical gradient algorithm that provides fast
convergence for large-scale problems. In the case of FISTA though, the regularization parameter λ

⁵Without dwelling into technicalities, for total variation, this equivalence is correct up to the constant, which is in the null space of the derivative operator.

⁶Again, this holds up to elements of the null space.

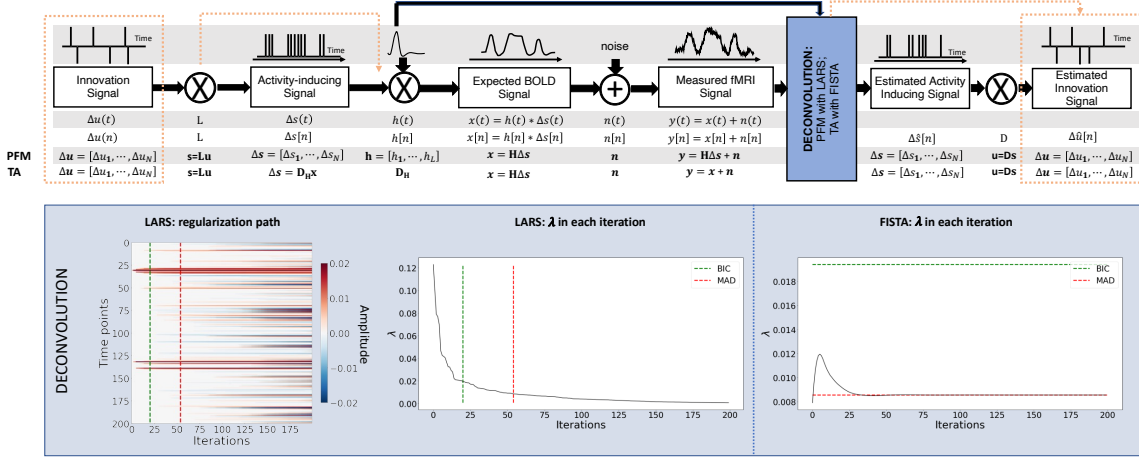


Figure 1: Flowchart detailing the different steps of the fMRI signal and the deconvolution methods described. The orange arrows indicate the flow to estimate the innovation signals, i.e., the derivative of the activity-inducing signal. The blue box depicts the iterative *modus operandi* of the two algorithms used in this paper to solve the paradigm free mapping (PFM) and total activation (TA) deconvolution problems. The plot on the left shows the regularization path obtained with the least angle regression (LARS) algorithm, where the x-axis illustrates the different iterations of the algorithm, the y-axis represents points in time, and the color describes the amplitude of the estimated signal. The middle plot depicts the decreasing values of λ for each iteration of LARS as the regularization path is computed. The green and red dashed lines in both plots illustrate the Bayesian information criterion (BIC) and median absolute deviation (MAD) solutions, respectively. Comparatively, the changes in λ when the fast iterative shrinkage-thresholding algorithm (FISTA) method is made to converge to the MAD estimate of the noise are shown on the right. Likewise, the λ corresponding to the BIC and MAD solutions are shown with dashed lines.

must be selected prior to solving the problem, but can be updated in every iteration so that the residuals of the data fit converge to an estimated noise level of the data $\hat{\sigma}$:

$$\lambda^{n+1} = \frac{N\hat{\sigma}}{\frac{1}{2}\|\mathbf{y} - \mathbf{x}^n\|_F^2} \lambda^n, \quad (8)$$

where x^n is the n^{th} iteration estimate, λ^n and λ^{n+1} are the n^{th} and $n+1^{th}$ iteration values for the regularization parameter λ , and N is the number of points in the time-course. The pre-estimated noise level can be obtained as the median absolute deviation (MAD) of the fine-scale wavelet coefficients (Daubechies, order 3) of the fMRI timecourse. The MAD criterion has been adopted in TA (17). Of note, similar formulations based on the MAD estimate have also been applied in PFM formulations (30, 69).

3. Methods

3.1. Simulated data

In order to compare the two methods while controlling for their correct performance, we created a simulation scenario that can be found in the GitHub repository shared in Section 6. For the sake of illustration, we describe here the simulations corresponding to a timecourse with a duration of 400 seconds (TR = 2 s) where the activity-inducing signal includes 5 events, which are convolved

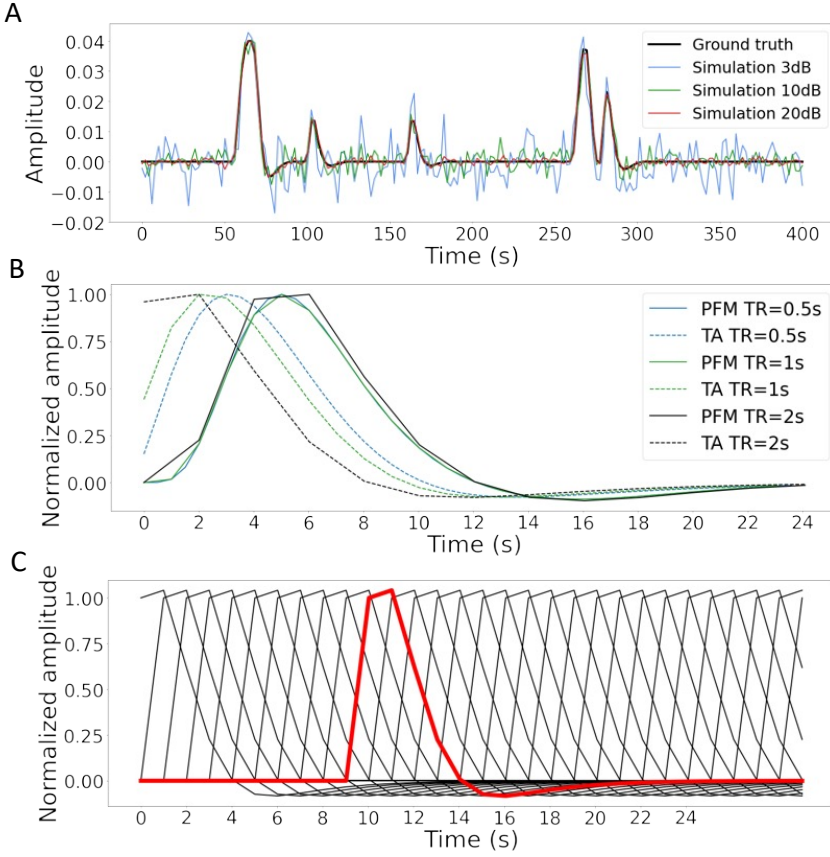


Figure 2: A) Simulated signal with different SNRs (20 dB, 10 dB and 3 dB) and ground truth given in signal percentage change (SPC). B) Canonical HRF models typically used by PFM (solid line) and TA (dashed line) at TR = 0.5 s (blue), TR = 1 s (green) and TR = 2 s (black). Without loss of generality, the waveforms are scaled to unit amplitude for visualization. C) Representation of shifted HRFs at TR = 2 s that build the design matrix for PFM when the HRF model has been matched to that in TA. The red line corresponds to one of the columns of the HRF matrix.

with the canonical HRF. Different noise sources (physiological, thermal, and motion-related) were also added and we simulated three different scenarios with varying signal-to-noise ratios (SNR = [20 dB, 10 dB, 3 dB]) that represent high, medium and low contrast-to-noise ratios as shown in Figure 2A. Noise was created following the procedure in (31) as the sum of uncorrelated Gaussian noise and sinusoidal signals to simulate a realistic noise model with thermal noise, cardiac and respiratory physiological fluctuations, respectively. The physiological signals were generated as

$$\sum_{i=1}^2 \frac{1}{2^{i-1}} (\sin(2\pi f_{r,i}t + \phi_{r,i}) + \sin(2\pi f_{c,i}t + \phi_{c,i})), \quad (9)$$

152 with up to second-order harmonics per cardiac ($f_{c,i}$) and respiratory ($f_{r,i}$) component that were
153 randomly generated following normal distributions with variance 0.04 and mean if_r and if_c , for
154 $i = [1, 2]$. We set the fundamental frequencies to $f_r = 0.3$ Hz for the respiratory component (70)
155 and $f_c = 1.1$ Hz for the cardiac component (71). The phases of each harmonic ϕ were randomly
156 selected from a uniform distribution between 0 and 2π radians. To simulate physiological noise that
157 is proportional to the change in BOLD signal, a variable ratio between the physiological (σ_P) and
158 the thermal (σ_0) noise was modeled as $\sigma_P/\sigma_0 = a(tSNR)^b + c$, where $a = 5.01 \times 10^{-6}$, $b = 2.81$,
159 and $c = 0.397$, following the experimental measures available in Table 3 from (72)).

160 *3.2. Experimental data*

161 To compare the performance of the two approaches as well as illustrate their operation, we
162 employ two representative experimental datasets.

163 **Motor task dataset:** One healthy subject was scanned in a 3T MR scanner (Siemens) under a
164 Basque Center on Cognition, Brain and Language Review Board-approved protocol. T2*-weighted
165 multi-echo fMRI data was acquired with a simultaneous-multislice multi-echo gradient echo-planar
166 imaging sequence, kindly provided by the Center of Magnetic Resonance Research (University of
167 Minnesota, USA) (73–75), with the following parameters: 340 time frames, 52 slices, Partial-Fourier
168 = 6/8, voxel size = $2.4 \times 2.4 \times 3$ mm 3 , TR = 1.5 s, TEs = 10.6/28.69/46.78/64.87/82.96 ms, flip
169 angle = 70°, multiband factor = 4, GRAPPA = 2.

170 During the fMRI acquisition, the subject performed a motor task consisting of five different
171 movements (left-hand finger tapping, right-hand finger tapping, moving the left toes, moving the
172 right toes and moving the tongue) that were visually cued through a mirror located on the head
173 coil. These conditions were randomly intermixed every 16 seconds, and were only repeated once
174 the entire set of stimuli were presented. Data preprocessing consisted of first, discarding the first 10
175 volumes of the functional data to achieve a steady state of magnetization. Then, image realignment
176 to the skull-stripped single-band reference image (SBRef) was computed on the first echo, and the
177 estimated rigid-body spatial transformation was applied to all other echoes (76, 77). A brain mask
178 obtained from the SBRef volume was applied to all the echoes and the different echo timeseries
179 were optimally combined (OC) voxelwise by weighting each timeseries contribution by its T2* value
180 (78). AFNI (79) was employed for a detrending of up to 4th-order Legendre polynomials, within-
181 brain spatial smoothing (3 mm FWHM) and voxelwise signal normalization to percentage change.
182 Finally, distortion field correction was performed on the OC volume with Topup (80), using the
183 pair of spin-echo EPI images with reversed phase encoding acquired before the ME-EPI acquisition
184 (81).

185 **Resting-state datasets:** One healthy subject was scanned in a 3T MR scanner (Siemens)
186 under a Basque Center on Cognition, Brain and Language Review Board-approved protocol. Two
187 runs of T2*-weighted fMRI data were acquired during resting-state, each with 10 min duration,
188 with 1) a standard gradient-echo echo-planar imaging sequence (monoband) (TR = 2000 ms, TE
189 = 29 ms, flip-angle = 78°, matrix size = 64 × 64, voxel size = 3 × 3 × 3 mm 3 , 33 axial slices
190 with interleaved acquisition, slice gap = 0.6 mm) and 2) a simultaneous-multislice gradient-echo
191 echo-planar imaging sequence (multiband factor = 3, TR = 800 ms, TE = 29 ms, flip-angle = 60°,
192 matrix size = 64 × 64, voxel size = 3 × 3 × 3 mm 3 , 42 axial slices with interleaved acquisition, no
193 slice gap). Single-band reference images were also collected in both resting-state acquisitions for
194 head motion realignment. Field maps were also obtained to correct for field distortions.

195 During both acquisitions, participants were instructed to keep their eyes open, fixating a white
196 cross that they saw through a mirror located on the head coil, and not to think about anything

197 specific. The data was pre-processed using AFNI (79). First, volumes corresponding to the initial
198 10 seconds were removed to allow for a steady-state magnetization. Then, the voxel time-series were
199 despiked to reduce large-amplitude deviations and slice-time corrected. Inhomogeneities caused by
200 magnetic susceptibility were corrected with FUGUE (FSL) using the field map images (76). Next,
201 functional images were realigned to a base volume (monoband: volume with the lowest head mo-
202 tion; multiband: single-band reference image). Finally, a simultaneous nuisance regression step
203 was performed comprising up to 6th-order Legendre polynomials, low-pass filtering with a cutoff
204 frequency of 0.25 Hz (only on multiband data to match the frequency content of the monoband), 6
205 realignment parameters plus temporal derivatives, 5 principal components of white matter (WM), 5
206 principal components of lateral ventricle voxels (anatomical CompCor) (82) and 5 principal compo-
207 nents of the brain's edge voxels ,(83). WM, CSF and brain's edge-voxel masks were obtained from
208 Freesurfer tissue and brain segmentations. In addition, scans with potential artifacts were identified
209 and censored when the euclidean norm of the temporal derivative of the realignment parameters
210 (ENORM) was larger than 0.4, and the proportion of voxels adjusted in the despiking step exceeded
211 10%.

212 *3.3. Selection of the hemodynamic response function*

213 In their original formulations, PFM and TA specify the discrete-time HRF in different ways.
214 For PFM, the continuous-domain specification of the canonical double-gamma HRF (57) is sampled
215 at the TR and then put as shifted impulse responses to build the matrix \mathbf{H} . In the case of TA,
216 however, the continuous-domain linearized version of the balloon-windkessel model is discretized to
217 build the linear differential operator in $\mathbf{D}_\mathbf{H}$. While the TR only changes the resolution of the HRF
218 shape for PFM, the impact of an equivalent impulse response of the discretized differential operator
219 at different TR is more pronounced. As shown in Figure 2B, longer TR leads to equivalent impulse
220 responses of TA that are shifted in time, provoking a lack of the initial baseline and rise of the
221 response. We refer the reader to Figure S1 to see the differences in the estimation of the activity-
222 inducing and innovation signals when both methods use the HRF in their original formulation.
223 To avoid differences between PFM and TA based on their built-in HRF, we choose to build the
224 synthesis operator \mathbf{H} with shifted versions of the HRF given by the TA analysis operator (e.g., see
225 Figure 2C for the TR=2s case).

226 *3.4. Selection of the regularization parameter*

227 We use the simulated data to compare the performance of the two deconvolution algorithms
228 with both BIC and MAD criteria to set the regularization parameter λ (see section 2.6). We also
229 evaluate if the algorithms behave differently in terms of the estimation of the activity-inducing
230 signal $\hat{\mathbf{s}}$ using the spike model described in (4) and the block model based on the innovation signal
231 $\hat{\mathbf{u}}$ in (7).

232 For selection based on the BIC, LARS was initially performed with the PFM deconvolution
233 model to obtain the solution for every possible λ in the regularization path. Then, the values of λ
234 corresponding to the BIC optimum were adopted to solve the TA deconvolution model by means
235 of FISTA.

236 For a selection based on the MAD estimate of the noise, we apply the temporal regularization in
237 its original form for TA, whereas for PFM the selected λ corresponds to the solution whose residuals
238 have the closest standard deviation to the estimated noise level of the data $\hat{\sigma}$.

239 *3.5. Analyses in experimental fMRI data*

Difference between approaches: To assess the discrepancies between both approaches when applied on experimental fMRI data, we calculate the square root of the sum of squares of the differences (RSSD) between the activity-inducing signals estimated with PFM and TA on the three experimental datasets as

$$\text{RSSD} = \sqrt{\frac{1}{N} \sum_{k=1}^N (\hat{s}_{\text{PFM}}[k] - \hat{s}_{\text{TA}}[k])^2}, \quad (10)$$

240 where N is the number of timepoints of the acquisition. The RSSD of the innovation signals $\hat{\mathbf{u}}$ was
241 computed equally.

242 **Task fMRI data:** In the analysis of the motor task data, we evaluate the performance of PFM
243 and TA in comparison with a conventional General Linear Model analysis (*3dDeconvolve* in AFNI)
244 that takes advantage of the information about the duration and onsets of the motor trials. Given
245 the block design of the motor task, we only make this comparison with the block model.

246 **Resting-state fMRI data:** We also illustrate the usefulness of deconvolution approaches in
247 the analysis of resting-state data where information about the timings of neuronal-related BOLD
248 activity cannot be predicted. Apart from being able to explore individual maps of deconvolved
249 activity (i.e., innovation signals, activity-inducing signals, or hemodynamic signals) at the temporal
250 resolution of the acquisition (or deconvolution), here we calculate the average extreme points of the
251 activity-inducing and innovation maps (given that these examples do not have a sufficient number of
252 scans to perform a clustering step) and illustrate how popular approaches like co-activation patterns
253 (CAPs)(84, 85) and innovation-driven co-activation patterns (iCAPs) (18) can be applied on the
254 deconvolved signals to reveal patterns of coordinated brain activity. To achieve this, we calculate
255 the average time-series in a seed of 9 voxels located in the precuneus, supramarginal gyrus, and
256 occipital gyri independently, and solve the deconvolution problem to find the activity-inducing
257 and innovation signals in the seeds. We then apply a 95th percentile threshold and average the
258 maps of the time-frames that survive the threshold. Finally, we apply the same procedure to the
259 original— i.e., non-deconvolved— signal in the seed and compare the results with the widely-used
260 seed correlation approach.

261 **4. Results**

262 *4.1. Performance based on the regularization parameter*

263 Figure 3A shows the regularization paths of PFM and TA side by side obtained for the spike
264 model of Eq. (4) for SNR=3 dB. The solutions for all three SNR conditions are shown in Figures S2
265 and S3. Starting from the maximum λ corresponding to a null estimate and for decreasing values
266 of λ , LARS computes a new estimate at the value of λ that reduces the sparsity promoted by the
267 l_1 -norm and causes a change in the active set of non-zero coefficients of the estimate (i.e., a zero
268 coefficient becomes non-zero or vice versa) as shown in the horizontal axis of the heatmaps. Vertical
269 dashed lines depict the selection of the regularization parameter based on the BIC, and thus, the
270 colored coefficients indicated by these depict the estimated activity-inducing signal $\hat{\mathbf{s}}$. Figure 3B
271 illustrates the resulting estimates of the activity-inducing and activity-related hemodynamic signals
272 when basing the selection of λ on the BIC for SNR=3 dB. Given that the regularization paths of
273 both approaches are identical, it can be clearly observed that the BIC-based estimates are identical
274 too for the corresponding λ . Thus, Figures 3A, 3B, S2 and S3 demonstrate that, regardless of

the simulated SNR condition, the spike model of both deconvolution algorithms produces identical regularization paths when the same HRF and regularization parameters are applied, and hence, identical estimates of the activity-inducing signal \hat{s} and neuronal-related hemodynamic signal \hat{x} . Likewise, Figure 3C demonstrates that the regularization paths for the block model defined in Eqs. (6) and (7) also yield virtually identical estimates of the innovation signals for both PFM and TA methods. Again, the BIC-based selection of λ is identical for both PFM and TA. As illustrated in Figure 3D, the estimates of the innovation signal u also show no distinguishable differences between the algorithms. Figures 3 A-D demonstrate that both PFM and TA yield equivalent regularization paths and estimates of the innovation signal and activity-inducing signal regardless of the simulated SNR condition when applying the same HRF and regularization parameters with the block and spike models.

As for selecting λ with the MAD criterion defined in Eq. (8), Figure 3E depicts the estimated activity-inducing and activity-related signals for the simulated low-SNR setting using the spike model, while Figure 3F shows the estimated signals corresponding to the block model. Both plots in Figure 3E and F depict nearly identical results between PFM and TA with both models. Given that the regularization paths of both techniques are identical, minor dissimilarities are owing to the slight differences in the selection of λ due to the quantization of the values returned by LARS.

4.2. Performance on experimental data

Figure 4 depicts the RSSD maps revealing differences between PFM and TA estimates for the spike (Figure 4A and C) and block (Figure 4B and D) models when applied to the three experimental fMRI datasets. The RSSD values are virtually negligible (i.e., depicted in yellow) in most of the within-brain voxels and lower than the amplitude of the estimates of the activity-inducing and innovation signals. Based on the maximum value of the range shown in each image, we observe that the similarity between both approaches is more evident for the spike model (with both selection criteria) and the block model with the BIC selection. However, given the different approaches used for the selection of the regularization parameter λ based on the MAD estimate of the noise (i.e., converging so that the residuals of FISTA are equal to the MAD estimate of the noise for TA vs. finding the LARS residual that is closest to the MAD estimate of the noise), higher RSSD values can be observed with the largest differences occurring in gray matter voxels. These areas also correspond to low values of λ (see Figure S4) and MAD estimates of the noise (see Figure S5), while the highest values are visible in regions with signal dropouts, ventricles, and white matter. These differences that arise from the differing methods to find the optimal regularization parameter based on the MAD estimate of the noise can be clearly seen in the root sum of squares (RSS) of the estimates of the two methods (Figure S6). These differences are also observable in the ATS calculated from estimates obtained with the MAD selection as shown in Figure S9. However, the identical regularization paths shown in Figure S7 demonstrate that both methods perform equivalently on experimental data (see estimates of innovation signal obtained with an identical selection of λ in Figure S8). Hence, the higher RSSD values originate from the different methods to find the optimal regularization parameter based on the MAD estimate of the noise that yield different solutions as shown by the dashed vertical lines in Figure S7.

Figure 5 depicts the results of the analysis of the Motor dataset with the PFM and TA algorithms using the BIC selection of λ (see Figure S9 for results with MAD selection), as well as a conventional GLM approach. The Activation Time Series (top left), calculated as the sum of squares of all voxel amplitudes (positive vs. negative) for a given moment in time, obtained with PFM and TA show nearly identical patterns. These ATS help to summarize the four dimensional information available

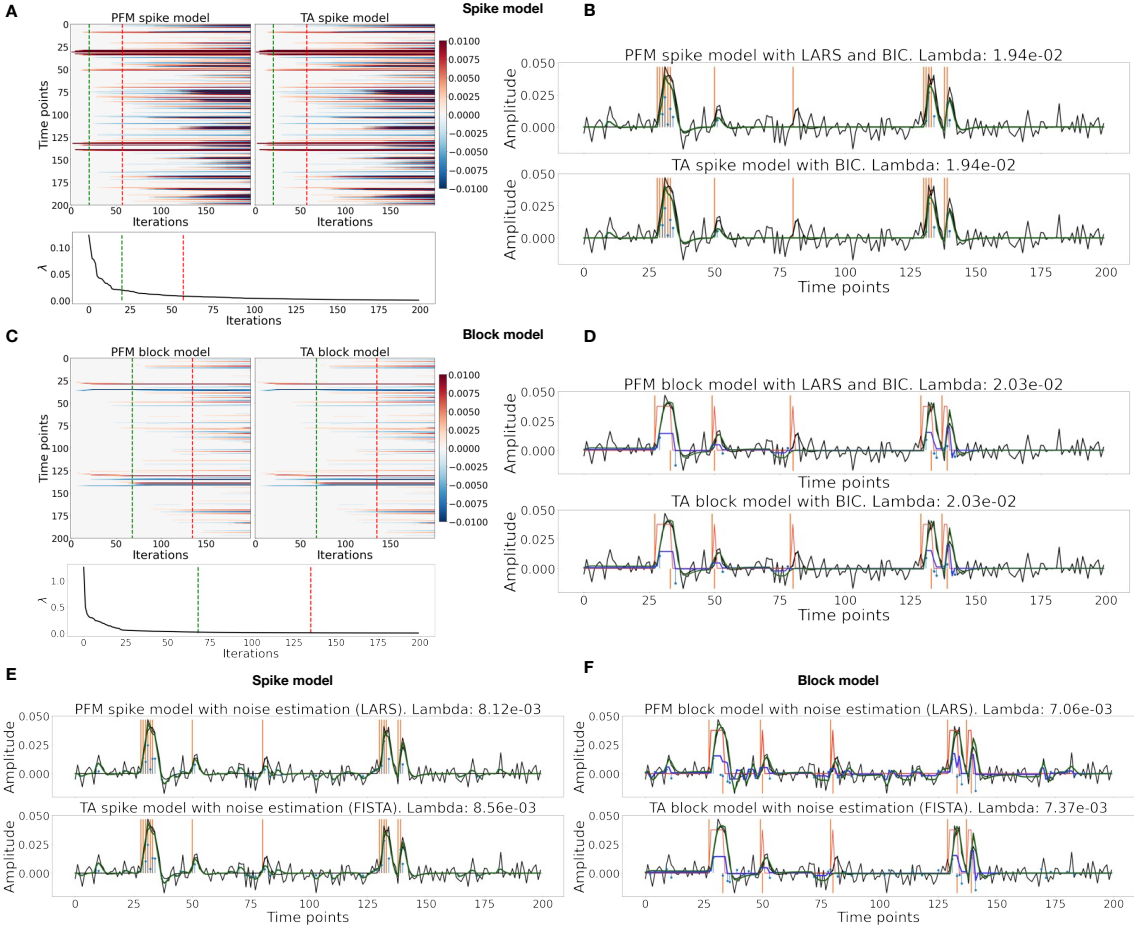


Figure 3: (A) Heatmap of the regularization paths of the activity-inducing signals (spike model) estimated with PFM and TA as a function of λ for the simulated data with SNR = 3 dB (x-axis: increasing number of iterations or λ as given by LARS; y-axis: time; color: amplitude). Vertical lines denote iterations corresponding to the BIC (dashed line) and MAD (dotted line) selection of λ . (B) Estimated activity-inducing (blue) and activity-related (green) signals with a selection of λ based on the BIC. Orange and red lines depict the ground truth. (C) Heatmap of the regularization paths of the innovation signals (block model) estimated with PFM and TA as a function of λ for the simulated data with SNR = 3 dB. (D) Estimated innovation (blue), activity-inducing (darker blue), and activity-related (green) signals with a selection of λ based on the BIC. (E) Activity-inducing and activity-related (fit, \times) signals estimated with PFM (top) and TA (bottom) when λ is selected based on the MAD method with the spike model, and (F) with the block model for the simulated data with SNR = 3 dB.

in the results across the spatial domain and identify instances of significant BOLD activity. The second to sixth rows show the voxel timeseries and the corresponding activity-related, activity-inducing and innovation signals obtained with PFM using the BIC criterion of representative voxels in the regions activated in each of the motor tasks. The TA-estimated time-series are not shown because they were virtually identical. The maps shown on the right correspond to statistical

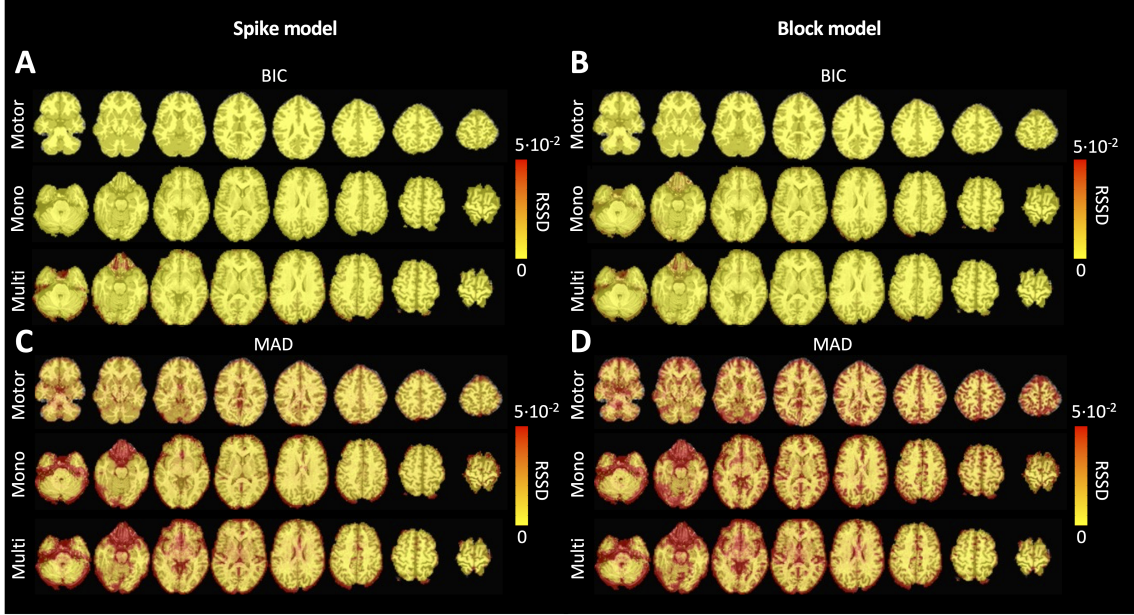


Figure 4: Square root of the sum of squared differences (RSSD) between the estimates obtained with PFM and TA for (A) spike model (activity-inducing signal) and BIC selection of λ , (B) block model (innovation signal) and BIC selection, (C) spike model (activity-inducing signal) and MAD selection, (D) block model (innovation signal) and MAD selection. RSSD maps are shown for the three experimental fMRI datasets: the motor task (Motor), the monoband resting-state (Mono), and the multiband resting-state (Multi) datasets.

parametric maps obtained with the GLM for each motor condition ($p < 0.001$) as well as the maps of the PFM and TA estimates at the onsets of individual motor events (indicated with arrows in the timecourses). The estimated activity-related, activity-inducing and innovation signals clearly reveal the activity patterns of each condition in the task, as they exhibit a BOLD response locked to the onset and duration of the conditions. Overall, activity maps of the innovation signal obtained with PFM and TA highly resemble those obtained with a GLM for individual events, with small differences arising from the distinct specificity of the GLM and deconvolution analyses. Notice that the differences observed with the different approaches to select λ based on the MAD estimate shown in Figure 4 are reflected on the ATS shown in Figure S9 as well.

As an illustration of the insights that deconvolution methods can provide in the analysis of resting-state data, Figure 6 depicts the average activity-inducing and innovation maps of common resting-state networks obtained from thresholding and averaging the activity-inducing and innovation signals, respectively, estimated from the resting-state multiband data using PFM with a selection of λ based on the BIC. The average activity-inducing maps obtained via deconvolution show spatial patterns of the default mode network (DMN), dorsal attention network (DAN), and visual network (VIS) that highly resemble the maps obtained with conventional seed correlation analysis using Pearson's correlation, and the average maps of extreme points of the signal (i.e., with no deconvolution). With deconvolution, the average activity-inducing maps seem to depict more accurate spatial delineation (i.e., less smoothness) than those obtained from the original data, while

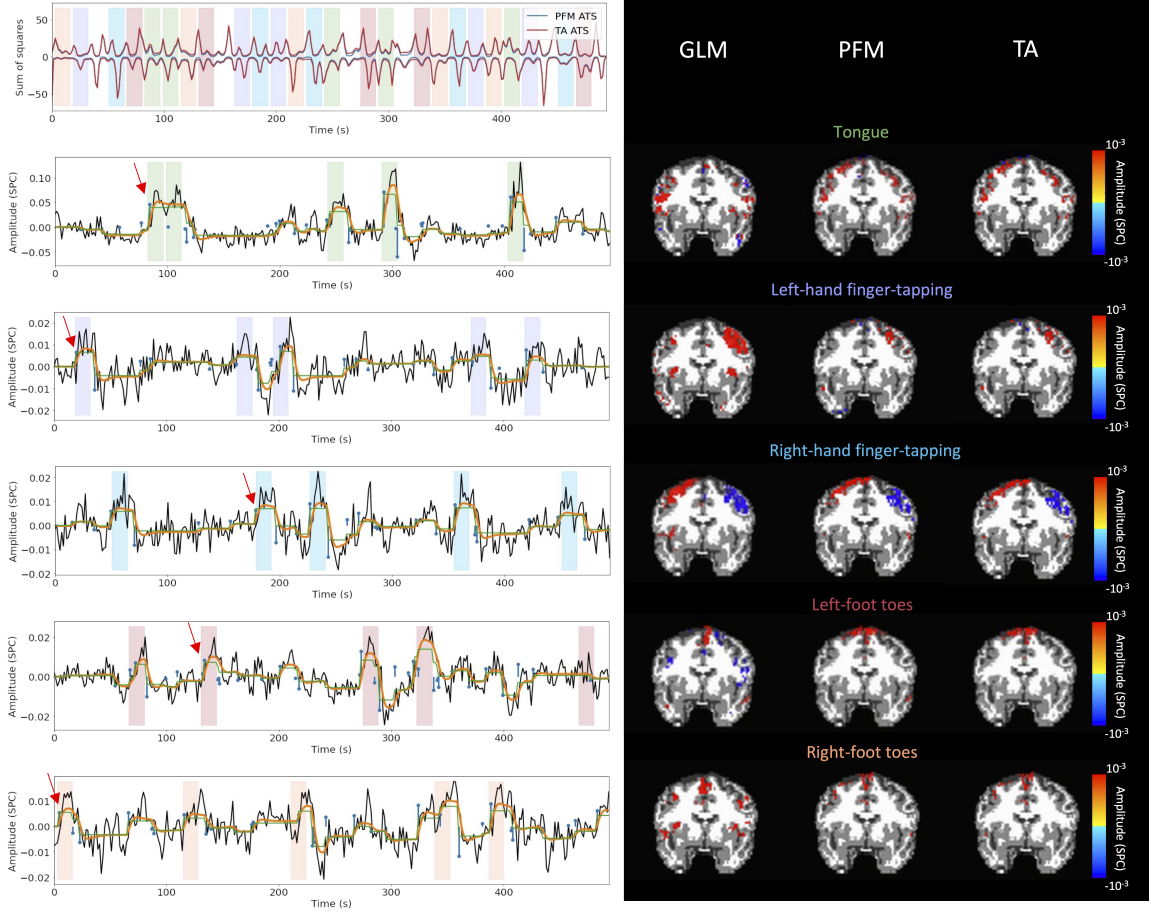


Figure 5: Activity maps of the motor task using a selection of λ based on the BIC estimate. Row 1: Activation time-series (ATS) of the innovation signals estimated by PFM (in blue) or TA (in red) calculated as the sum of squares of all voxels at every timepoint. Positive-valued and negative-valued contributions were separated into two distinct time-courses. Color-bands indicate the onset and duration of each condition in the task (green: tongue motion, purple: left-hand finger-tapping, blue: right-hand finger-tapping, red: left-foot toes motion, orange: right-foot toes motion). Rows 2-6: time-series of a representative voxel for each task with the PFM-estimated innovation (blue), PFM-estimated activity-inducing (green), and activity-related (i.e., fitted, orange) signals, with their corresponding GLM, PFM, and TA maps on the right (representative voxels indicated with green arrows). Amplitudes are given in signal percentage change (SPC). The maps shown on the right are sampled at the time-points labeled with the red arrows and display the innovation signals at these moments across the whole brain.

344 maintaining the structure of the networks. The BIC-informed selection of λ yields spatial patterns
 345 of average activity-inducing and innovation maps that are more sparse than those obtained with a
 346 selection of λ based on the MAD estimate (see Figure S10). Furthermore, the spatial patterns of
 347 the average innovation maps based on the innovation signals using the block model yield comple-
 348 mentary information to those obtained with the activity-inducing signal since iCAPs allow to reveal
 349 regions with synchronous innovations, i.e., with the same upregulating and downregulating events.

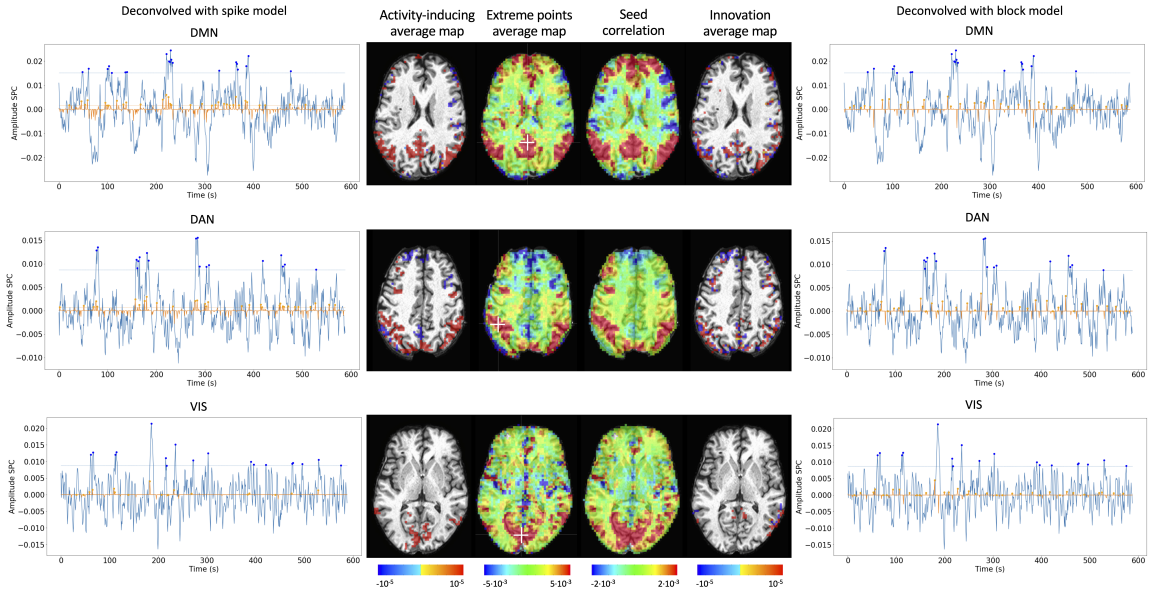


Figure 6: Average activity-inducing (left) and innovation (right) maps obtained from PFM-estimated activity-inducing and innovation signals, respectively, using a BIC-based selection of λ . Time-points selected with a 95th percentile threshold (horizontal lines) are shown over the average time-series (blue) in the seed region (white cross) and the deconvolved signals, i.e., activity inducing (left) and innovation (right) signals (orange). Average maps of extreme points and seed correlation maps are illustrated in the center.

350 For instance, it is interesting to observe that the structure of the visual network nearly disappears in
 351 its corresponding average innovation maps, suggesting the existence of different temporal neuronal
 352 patterns across voxels in the primary and secondary visual cortices.

353 5. Discussion and conclusion

354 Hemodynamic deconvolution can be formulated using a synthesis- and analysis-based approach
 355 as proposed by PFM and TA, respectively. This work demonstrates that the theoretical equivalence
 356 of both approaches is confirmed in practice given virtually identical results when the same HRF
 357 model and equivalent regularization parameters are employed. Hence, we argue that previously ob-
 358 served differences in performance can be explained by specific settings, such as the HRF model and
 359 selection of the regularization parameter (as shown in Figures 4,S6 and S7), convergence thresholds,
 360 as well as the addition of a spatial regularization term in the spatiotemporal TA formulation (17).
 361 For instance, the use of PFM with the spike model in (23) was seen not to be ideal due to the
 362 prolonged trials in the paradigm, which better fit the block model as described here (7). However,
 363 given the equivalence of the temporal deconvolution, incorporating extra spatial or temporal regu-
 364 larization terms in the optimization problem should not modify this equivalence providing convex
 365 operators are employed. For a convex optimization problem, with a unique global solution, iterative
 366 shrinkage thresholding procedures alternating between the different regularization terms guarantee
 367 convergence; e.g., the generalized forward-backward splitting (86) algorithm originally employed

for TA. Our findings are also in line with the equivalence of analysis and synthesis methods in under-determined cases ($N \leq V$) demonstrated in (50) and (51). Still, we have shown that a slight difference in the selection of the regularization parameter can lead to small differences in the estimated signals when employing the block model with the MAD selection of λ . However, since their regularization paths are equivalent, the algorithms can easily be forced to converge to the same selection of λ , thus resulting in identical estimated signals.

Nevertheless, the different formulations of analysis and synthesis deconvolution models bring along different kinds of flexibility. One notable advantage of PFM is that it can readily incorporate any HRF as part of the synthesis operator (50), only requiring the sampled HRF at the desired temporal resolution, which is typically equal to the TR of the acquisition. Conversely, TA relies upon the specification of the discrete differential operator that inverts the HRF, which needs to be derived either by the inverse solution of the sampled HRF impulse response, or by discretizing a continuous-domain differential operator motivated by a biophysical model. The more versatile structure of PFM allows for instance an elegant extension of the algorithm to multi-echo fMRI data (32) where multiple measurements relate to a common underlying signal. Therefore, the one-to-many synthesis scenario (i.e., from activity-inducing to several activity-related signals) is more cumbersome to express using TA; i.e., a set of differential operators should be defined and the differences between their outputs constrained. Conversely, the one-to-many analysis scenario (i.e., from the measurements to several regularizing signals) is more convenient to be expressed by TA; e.g., combining spike and block regularizers. While the specification of the differential operator in TA only indirectly controls the HRF, the use of the derivative operator to enforce the block model, instead of the integrator in PFM, impacts positively the stability and rate of the convergence of the optimization algorithms. Moreover, analysis formulations can be more suitable for online applications that are still to be explored in fMRI data, but are employed for calcium imaging deconvolution (87, 88), and which have been applied for offline calcium deconvolution (89).

Deconvolution techniques can be used before more downstream analysis of brain activity in terms of functional network organization as they estimate interactions between voxels or brain regions that occur at the activity-inducing level, and are thus less affected by the slowness of the hemodynamic response compared to when the BOLD signals are analyzed directly. In addition, deconvolution approaches hold a close parallelism to recent methodologies aiming to understand the dynamics of neuronal activations and interactions at short temporal resolution and that focus on extreme events of the fMRI signal (90). As an illustration, Figure 6 shows that the innovation- or activity-inducing CAPs computed from deconvolved events in a single resting-state fMRI dataset closely resemble the conventional CAPs computed directly from extreme events of the fMRI signal (84, 85, 91–98). Similarly, we hypothesize that these extreme events will also show a close resemblance to intrinsic ignition events (99, 100). As shown in the maps, deconvolution approaches can offer a more straightforward interpretability of the activation events and resulting functional connectivity patterns. Here, CAPs were computed as the average of spatial maps corresponding to the events of a single dataset. Beyond simple averaging, clustering algorithms (e.g., K-means and consensus clustering) can be employed to discern multiple CAPs or iCAPs at the whole-brain level for a large number of subjects. Previous findings based on iCAPs have for instance revealed organizational principles of brain function during rest (18) and sleep (28) in healthy controls, next to alterations in 22q11ds (25) and multiple sclerosis (24). Next to CAPs-inspired approaches, dynamic functional connectivity has recently been investigated with the use of co-fluctuations and edge-centric techniques (101–105). The activation time series shown in Figure 5 aim to provide equivalent information to the root of sum of squares timecourses used in edge-centric approaches,

414 where timecourses with peaks delineate instances of significant brain activity. Future work could
415 address which type of information is redundant or distinct across these frameworks. In summary,
416 these examples illustrate that deconvolution techniques can be employed prior to other computa-
417 tional approaches and could serve as an effective way of denoising the fMRI data. We foresee an
418 increase in the number of studies that take advantage of the potential benefits of using deconvolution
419 methods prior to functional connectivity analyses.

420 In sum, hemodynamic deconvolution approaches using sparsity-driven regularization are valua-
421 ble tools to complete the fMRI processing pipeline. Although the two approaches examined in
422 detail here provide alternative representations of the BOLD signals in terms of innovation and
423 activity-inducing signals, their current implementations have certain limitations, calling for further
424 developments or more elaborate models, where some of them have been initially addressed in the
425 literature. One relevant focus is to account for the variability in HRF that can be observed in
426 different regions of the brain. First, variability in the temporal characteristics of the HRF can arise
427 from differences in stimulus intensity and patterns, as well as with short inter-event intervals like in
428 fast cognitive processes or experimental designs (106–109). Similarly, the HRF shape at rest might
429 differ from the canonical HRF commonly used for task-based fMRI data analysis. A wide variety of
430 HRF patterns could be elicited across the whole brain and possible detected with sufficiently large
431 signal-to-noise ratio, e.g., (110) showed two gamma-shaped responses at the onset and the end of
432 the evoked trial, respectively. This unique HRF shape would be deconvolved as two separate events
433 with the conventional deconvolution techniques. The impact of HRF variability could be reduced
434 using structured regularization terms along with multiple basis functions (30) or procedures that
435 estimate the HRF shape in an adaptive fashion in both analysis (111) and synthesis formulations
436 (112).

437 Another avenue of research consists in leveraging spatial information by adopting multivariate
438 deconvolution approaches that operate at the whole-brain level, instead of working voxelwise and
439 beyond regional regularization terms (e.g. as proposed in (author?) 17). Operating at the whole-
440 brain level would open the way for methods that consider shared neuronal activity using mixed
441 norm regularization terms (113) or can capture long-range neuronal cofluctuations using low rank
442 decompositions (112). For example, multivariate deconvolution approaches could yield better local-
443 ized activity patterns while reducing the effect of global fluctuations such as respiratory artifacts,
444 which cannot be modelled at the voxel level (114).

445 Similar to solving other inverse problems by means of regularized estimators, the selection of
446 the regularization parameter is critical to correctly estimate the neuronal-related signal. Hence,
447 methods that take advantage of a more robust selection of the regularization parameter could
448 considerably yield more reliable estimates of the neuronal-related signal. For instance, the stabili-
449 ty selection (65, 115) procedure could be included to the deconvolution problem to ensure that
450 the estimated coefficients are obtained with high probability. Furthermore, an important issue of
451 regularized estimation is that the estimates are biased with respect to the true value. In that
452 sense, the use of non-convex $\ell_{p,q}$ -norm regularization terms (e.g., $p < 1$) can reduce this bias while
453 maintaining the sparsity constraint, at the cost of potentially converging to a local minima of the
454 regularized estimation problem. In practice, these approaches could avoid the optional debiasing
455 step that overcomes the shrinkage of the estimates and obtain a more accurate and less biased fit
456 of the fMRI signal (31, 32). Finally, cutting-edge developments on physics-informed deep learning
457 techniques for inverse problems (116–119) could be transferred for deconvolution by considering the
458 biophysical model of the hemodynamic system and could potentially offer algorithms with reduced
459 computational time and more flexibility.

460 **6. Code and data availability**

461 The code and materials used in this work can be found in the following GitHub repository:
462 https://github.com/eurunuela/pfm_vs_ta. We encourage the reader to explore the parameters
463 (e.g., SNR, varying HRF options and mismatch between algorithms, TR, number of events, onsets,
464 and durations) in the provided Jupyter notebooks. Likewise, the data used to produce the figures
465 can be found in <https://osf.io/f3ryg/>.

466 **7. Acknowledgements**

467 We thank Stefano Moia and Vicente Ferrer for data availability, and Younes Farouj for valuable
468 comments on the manuscript. This research was funded by the Spanish Ministry of Economy and
469 Competitiveness (RYC-2017-21845), the Basque Government (BERC 2018-2021, PIB_2019_104,
470 PRE_2020_2_0227), and the Spanish Ministry of Science, Innovation and Universities (PID2019-
471 105520GB-100), and the Swiss National Science Foundation (grant 205321_163376).

472 **8. CRediT**

473 Eneko Uruñuela: Conceptualisation, Methodology, Software, Formal Analysis, Investigation,
474 Data Curation, Writing (OD), Writing (RE), Visualisation, Funding acquisition. Thomas A.W.
475 Bolton: Conceptualisation, Methodology, Writing (RE). Dimitri Van de Ville: Conceptualisation,
476 Methodology, Writing (RE). César Caballero-Gaudes: Conceptualisation, Methodology, Software,
477 Formal Analysis, Investigation, Data Curation, Writing (OD), Writing (RE), Visualisation, Funding
478 acquisition.

479 **References**

- 480 1 Goutte C, Nielsen FA, Hansen LK. Modeling the haemodynamic response in fMRI using
481 smooth FIR filters. IEEE transactions on medical imaging. 2000 Dec;19:1188-201.
- 482 2 Marrelec G, Benali H, Ciuci P, Poline JB. Bayesian estimation of the hemodynamic response
483 function in functional MRI. AIP Conference Proceedings. 2002;617(1):229-47.
- 484 3 Ciuci P, Poline JB, Marrelec G, Idier J, Pallier C, Benali H. Unsupervised robust nonpara-
485 metric estimation of the hemodynamic response function for any fMRI experiment. IEEE
486 transactions on medical imaging. 2003 Oct;22:1235-51.
- 487 4 Casanova R, Ryali S, Serences J, Yang L, Kraft R, Laurienti PJ, et al. The impact of temporal
488 regularization on estimates of the BOLD hemodynamic response function: A comparative
489 analysis. NeuroImage. 2008 may;40(4):1606-18.
- 490 5 Glover GH. Deconvolution of Impulse Response in Event-Related BOLD fMRI1. NeuroImage.
491 1999 apr;9(4):416-29.
- 492 6 Gitelman DR, Penny WD, Ashburner J, Friston KJ. Modeling regional and psychophysio-
493 logic interactions in fMRI: the importance of hemodynamic deconvolution. NeuroImage. 2003
494 may;19(1):200-7.

- 495 7 Gerchen MF, Bernal-Casas D, Kirsch P. Analyzing task-dependent brain network changes by
496 whole-brain psychophysiological interactions: A comparison to conventional analysis. *Human*
497 *Brain Mapping*. 2014 apr;35(10):5071-82.
- 498 8 Di X, Biswal BB. Toward Task Connectomics: Examining Whole-Brain Task Modulated
499 Connectivity in Different Task Domains. *Cerebral Cortex*. 2018 jun;29(4):1572-83.
- 500 9 Freitas LGA, Bolton TAW, Krikler BE, Jochaut D, Giraud AL, Hüppi PS, et al. Time-resolved
501 effective connectivity in task fMRI: Psychophysiological interactions of Co-Activation patterns.
502 *NeuroImage*. 2020 may;212:116635.
- 503 10 Preti MG, Bolton TA, Van De Ville D. The dynamic functional connectome: State-of-the-art
504 and perspectives. *NeuroImage*. 2017 oct;160:41-54.
- 505 11 Keilholz S, Caballero-Gaudes C, Bandettini P, Deco G, Calhoun V. Time-Resolved Resting-
506 State Functional Magnetic Resonance Imaging Analysis: Current Status, Challenges, and New
507 Directions. *Brain Connectivity*. 2017 oct;7(8):465-81.
- 508 12 Lurie DJ, Kessler D, Bassett DS, Betzel RF, Breakspear M, Kheilholz S, et al. Questions and
509 controversies in the study of time-varying functional connectivity in resting fMRI. *Network*
510 *Neuroscience*. 2020 jan;4(1):30-69.
- 511 13 Bolton TAW, Morgenroth E, Preti MG, Van De Ville D. Tapping into Multi-Faceted Human
512 Behavior and Psychopathology Using fMRI Brain Dynamics. *Trends in Neurosciences*. 2020
513 sep;43(9):667-80.
- 514 14 Karahanoğlu FI, Van De Ville D. Dynamics of large-scale fMRI networks: Deconstruct brain
515 activity to build better models of brain function. *Current Opinion in Biomedical Engineering*.
516 2017 sep;3:28-36.
- 517 15 Petridou N, Gaudes CC, Dryden IL, Francis ST, Gowland PA. Periods of rest in fMRI contain
518 individual spontaneous events which are related to slowly fluctuating spontaneous activity.
519 *Human Brain Mapping*. 2012 feb;34(6):1319-29.
- 520 16 Allan TW, Francis ST, Caballero-Gaudes C, Morris PG, Liddle EB, Liddle PF, et al. Functional
521 Connectivity in MRI Is Driven by Spontaneous BOLD Events. *PLOS ONE*. 2015
522 apr;10(4):e0124577.
- 523 17 Karahanoğlu FI, Caballero-Gaudes C, Lazeyras F, Van De Ville D. Total activation: fMRI
524 deconvolution through spatio-temporal regularization. *NeuroImage*. 2013 jun;73:121-34.
- 525 18 Karahanoğlu FI, Van De Ville D. Transient brain activity disentangles fMRI resting-state
526 dynamics in terms of spatially and temporally overlapping networks. *Nature Communications*.
527 2015 jul;6(1):7751.
- 528 19 Kinany N, Pirondini E, Micera S, Van De Ville D. Dynamic Functional Connectivity of
529 Resting-State Spinal Cord fMRI Reveals Fine-Grained Intrinsic Architecture. *Neuron*. 2020
530 nov;108(3):424-35.e4.
- 531 20 Di X, Biswal BB. Modulatory Interactions of Resting-State Brain Functional Connectivity.
532 *PLoS ONE*. 2013 aug;8(8):e71163.

- 533 21 Di X, Biswal BB. Characterizations of resting-state modulatory interactions in the human
534 brain. *Journal of Neurophysiology*. 2015 nov;114(5):2785-96.
- 535 22 Gonzalez-Castillo J, Caballero-Gaudes C, Topolski N, Handwerker DA, Pereira F, Bandettini
536 PA. Imaging the spontaneous flow of thought: Distinct periods of cognition contribute to
537 dynamic functional connectivity during rest. *NeuroImage*. 2019 nov;202:116129.
- 538 23 Tan FM, Caballero-Gaudes C, Mullinger KJ, Cho SY, Zhang Y, Dryden IL, et al. Decoding
539 fMRI events in sensorimotor motor network using sparse paradigm free mapping and activation
540 likelihood estimates. *Human Brain Mapping*. 2017 aug;38(11):5778-94.
- 541 24 Bommarito G, Tarun A, Farouj Y, Preti MG, Petracca M, Droby A, et al. Altered anterior
542 default mode network dynamics in progressive multiple sclerosis. *Multiple Sclerosis Journal*.
543 2021 jun;28(2):206-16.
- 544 25 Zoeller D, Sandini C, Karahanoglu FI, Schaer M, Eliez S, Van De Ville D. Large-Scale Brain
545 Network Dynamics Provide a Measure of Psychosis and Anxiety in 22q11.2 Deletion Syndrome.
546 *Biological Psychiatry: Cognitive Neuroscience and Neuroimaging*. 2019;4:881-92.
- 547 26 Lopes R, Lina JM, Fahoum F, Gotman J. Detection of epileptic activity in fMRI without
548 recording the EEG. *NeuroImage*. 2012 apr;60(3):1867-79.
- 549 27 Karahanoglu FI, Grouiller F, Gaudes CC, Seeck M, Vulliemoz S, Van De Ville D. Spatial
550 mapping of interictal epileptic discharges in fMRI with total activation. In: 2013 IEEE 10th
551 International Symposium on Biomedical Imaging. Ieee. IEEE; 2013. p. 1500-3.
- 552 28 Tarun A, Wainstein-Andriano D, Sterpenich V, Bayer L, Perogamvros L, Solms M, et al. NREM
553 sleep stages specifically alter dynamical integration of large-scale brain networks. *Iscience*. 2020
554 jul;24(1):101923.
- 555 29 Gaudes CC, Petridou N, Dryden IL, Bai L, Francis ST, Gowland PA. Detection and character-
556 ization of single-trial fMRI bold responses: Paradigm free mapping. *Human Brain Mapping*.
557 2010 oct;32(9):1400-18.
- 558 30 Gaudes CC, Karahanoglu FI, Lazeyras F, Van De Ville D. Structured sparse deconvolution for
559 paradigm free mapping of functional MRI data. In: 2012 9th IEEE International Symposium
560 on Biomedical Imaging (ISBI). IEEE. IEEE; 2012. p. 322-5.
- 561 31 Gaudes CC, Petridou N, Francis ST, Dryden IL, Gowland PA. Paradigm free mapping
562 with sparse regression automatically detects single-trial functional magnetic resonance imaging
563 blood oxygenation level dependent responses. *Human Brain Mapping*. 2013:n/a-n/a.
- 564 32 Caballero-Gaudes C, Moia S, Panwar P, Bandettini PA, Gonzalez-Castillo J. A deconvolution
565 algorithm for multi-echo functional MRI: Multi-echo Sparse Paradigm Free Mapping. *Neu-
566 roImage*. 2019 nov;202:116081.
- 567 33 Hernandez-Garcia L, Ulfarsson MO. Neuronal event detection in fMRI time series using iter-
568 ative deconvolution techniques. *Magnetic Resonance Imaging*. 2011 apr;29(3):353-64.
- 569 34 Cherkaoui H, Moreau T, Halimi A, Ciuciu P. Sparsity-based Blind Deconvolution of Neu-
570 ral Activation Signal in fMRI. In: ICASSP 2019 - 2019 IEEE International Conference on
571 Acoustics, Speech and Signal Processing (ICASSP). IEEE; 2019. p. 1323-7.

- 572 35 Hütel M, Antonelli M, Melbourne A, Ourselin S. Hemodynamic matrix factorization for func-
573 tional magnetic resonance imaging. *NeuroImage*. 2021 may;231:117814.
- 574 36 Costantini I, Deriche R, Deslauriers-Gauthier S. An Anisotropic 4D Filtering Approach to Re-
575 cover Brain Activation From Paradigm-Free Functional MRI Data. *Frontiers in Neuroimaging*.
576 2022 apr;1.
- 577 37 Bush K, Cisler J. Decoding neural events from fMRI BOLD signal: A comparison of ex-
578 isting approaches and development of a new algorithm. *Magnetic Resonance Imaging*. 2013
579 jul;31(6):976-89.
- 580 38 Bush K, Zhou S, Cisler J, Bian J, Hazaroglu O, Gillispie K, et al. A deconvolution-based
581 approach to identifying large-scale effective connectivity. *Magnetic Resonance Imaging*. 2015
582 dec;33(10):1290-8.
- 583 39 Loula J, Varoquaux G, Thirion B. Decoding fMRI activity in the time domain improves
584 classification performance. *NeuroImage*. 2018 oct;180:203-10.
- 585 40 Pidnebesna A, Fajnerová I, Horáček J, Hlinka J. Estimating Sparse Neuronal Signal from
586 Hemodynamic Response: the Mixture Components Inference Approach. *bioRxiv*. 2019 dec.
- 587 41 Hütel M, Melbourne A, Ourselin S. Neural Activation Estimation in Brain Networks During
588 Task and Rest Using BOLD-fMRI. In: *Medical Image Computing and Computer Assisted
589 Intervention – MICCAI 2018*. Springer. Springer International Publishing; 2018. p. 215-22.
- 590 42 Sreenivasan KR, Havlicek M, Deshpande G. Nonparametric Hemodynamic Deconvolu-
591 tion of fMRI Using Homomorphic Filtering. *IEEE Transactions on Medical Imaging*. 2015
592 may;34(5):1155-63.
- 593 43 Riera JJ, Watanabe J, Kazuki I, Naoki M, Aubert E, Ozaki T, et al. A state-space model of the
594 hemodynamic approach: nonlinear filtering of BOLD signals. *NeuroImage*. 2004 feb;21(2):547-
595 67.
- 596 44 Penny W, Ghahramani Z, Friston K. Bilinear dynamical systems. *Philosophical Transactions
597 of the Royal Society B: Biological Sciences*. 2005 may;360(1457):983-93.
- 598 45 Friston KJ, Trujillo-Barreto N, Daunizeau J. DEM: A variational treatment of dynamic sys-
599 tems. *NeuroImage*. 2008 jul;41(3):849-85.
- 600 46 Havlicek M, Friston KJ, Jan J, Brazdil M, Calhoun VD. Dynamic modeling of neuronal
601 responses in fMRI using cubature Kalman filtering. *NeuroImage*. 2011 jun;56(4):2109-28.
- 602 47 Aslan S, Cemgil AT, Akin A. Joint state and parameter estimation of the hemodynamic model
603 by particle smoother expectation maximization method. *Journal of Neural Engineering*. 2016
604 jun;13(4):046010.
- 605 48 Madi MK, Karameh FN. Hybrid Cubature Kalman filtering for identifying nonlinear
606 models from sampled recording: Estimation of neuronal dynamics. *PLOS ONE*. 2017
607 jul;12(7):e0181513.
- 608 49 Ruiz-Euler HC, Marques JRF, Kappen HJ. Nonlinear Deconvolution by Sampling Biophysically
609 Plausible Hemodynamic Models. *arXiv*; 2018.

- 610 50 Elad M, Milanfar P, Rubinstein R. Analysis versus synthesis in signal priors. *Inverse Problems*.
 611 2007 apr;23(3):947-68.
- 612 51 Ortelli F, van de Geer S. Synthesis and analysis in total variation regularization; 2019.
- 613 52 Karahanoglu FI, Bayram İ, Van De Ville D. A Signal Processing Approach to Generalized 1-D
 614 Total Variation. *IEEE Transactions on Signal Processing*. 2011 nov;59(11):5265-74.
- 615 53 Friston KJ, Jezzard P, Turner R. Analysis of functional MRI time-series. *Human Brain
 616 Mapping*. 1994;1(2):153-71.
- 617 54 Friston KJ, Fletcher P, Josephs O, Holmes A, Rugg MD, Turner R. Event-Related fMRI:
 618 Characterizing Differential Responses. *NeuroImage*. 1998 jan;7(1):30-40.
- 619 55 Boynton GM, Engel SA, Glover GH, Heeger DJ. Linear Systems Analysis of Functional Mag-
 620 netic Resonance Imaging in Human V1. *The Journal of Neuroscience*. 1996 jul;16(13):4207-21.
- 621 56 Cohen MS. Parametric Analysis of fMRI Data Using Linear Systems Methods. *NeuroImage*.
 622 1997 aug;6(2):93-103.
- 623 57 Henson R, Friston K. CHAPTER 14 - Convolution Models for fMRI. In: Friston K, Ashburner
 624 J, Kiebel S, Nichols T, Penny W, editors. *Statistical Parametric Mapping*. London: Academic
 625 Press; 2007. p. 178-92.
- 626 58 Bruckstein AM, Donoho DL, Elad M. From Sparse Solutions of Systems of Equations to Sparse
 627 Modeling of Signals and Images. *SIAM Review*. 2009 feb;51(1):34-81.
- 628 59 Chen SS, Donoho DL, Saunders MA. Atomic decomposition by basis pursuit. *SIAM review*.
 629 2001;43(1):129-59.
- 630 60 Tibshirani R. Regression Shrinkage and Selection Via the Lasso. *Journal of the Royal Statistical
 631 Society: Series B (Methodological)*. 1996 jan;58(1):267-88.
- 632 61 Chambolle A. An algorithm for total variation minimization and applications. *Journal of
 633 Mathematical imaging and vision*. 2004;20(1):89-97.
- 634 62 Buxton RB, Wong EC, Frank LR. Dynamics of blood flow and oxygenation changes during
 635 brain activation: the balloon model. *Magnetic resonance in medicine*. 1998;39(6):855-64.
- 636 63 Friston KJ, Mechelli A, Turner R, Price CJ. Nonlinear responses in fMRI: the Balloon model,
 637 Volterra kernels, and other hemodynamics. *NeuroImage*. 2000;12(4):466-77.
- 638 64 Khalidov I, Fadili J, Lazeyras F, Van De Ville D, Unser M. Activelets: Wavelets for sparse
 639 representation of hemodynamic responses. *Signal Processing*. 2011 dec;91(12):2810-21.
- 640 65 Uruñuela E, Jones S, Crawford A, Shin W, Oh S, Lowe M, et al. Stability-Based Sparse
 641 Paradigm Free Mapping Algorithm for Deconvolution of Functional MRI Data. *Proceedings of
 642 the Annual International Conference of the IEEE Engineering in Medicine and Biology Society,
 643 EMBS*. 2020 jul;2020-July:1092-5.
- 644 66 Efron B, Hastie T, Johnstone I, Tibshirani R. Least angle regression. *The Annals of Statistics*.
 645 2004 apr;32(2):407-99.

- 646 67 Beck A, Teboulle M. A Fast Iterative Shrinkage-Thresholding Algorithm for Linear Inverse
647 Problems. SIAM Journal on Imaging Sciences. 2009 jan;2(1):183-202.
- 648 68 Schwarz G. Estimating the Dimension of a Model. The Annals of Statistics. 1978 mar;6(2):461-
649 4.
- 650 69 Gaudes CC, Van De Ville D, Petridou N, Lazeyras F, Gowland P. Paradigm-free mapping with
651 morphological component analysis: Getting most out of fMRI data. In: Wavelets and Sparsity
652 XIV. vol. 8138. International Society for Optics and Photonics; 2011. p. 81381K.
- 653 70 Birn RM, Diamond JB, Smith MA, Bandettini PA. Separating respiratory-variation-
654 related fluctuations from neuronal-activity-related fluctuations in fMRI. NeuroImage. 2006
655 jul;31(4):1536-48.
- 656 71 Shmueli K, van Gelderen P, de Zwart JA, Horovitz SG, Fukunaga M, Jansma JM, et al. Low-
657 frequency fluctuations in the cardiac rate as a source of variance in the resting-state fMRI
658 BOLD signal. NeuroImage. 2007 nov;38(2):306-20.
- 659 72 Triantafyllou C, Hoge RD, Krueger G, Wiggins CJ, Potthast A, Wiggins GC, et al. Comparison
660 of physiological noise at 1.5 T, 3 T and 7 T and optimization of fMRI acquisition parameters.
661 NeuroImage. 2005 may;26(1):243-50.
- 662 73 Feinberg DA, Moeller S, Smith SM, Auerbach E, Ramanna S, Glasser MF, et al. Multiplexed
663 Echo Planar Imaging for Sub-Second Whole Brain fMRI and Fast Diffusion Imaging. PLoS
664 ONE. 2010 dec;5(12):e15710.
- 665 74 Moeller S, Yacoub E, Olman CA, Auerbach E, Strupp J, Harel N, et al. Multiband multi-
666 slice GE-EPI at 7 tesla, with 16-fold acceleration using partial parallel imaging with applica-
667 tion to high spatial and temporal whole-brain fMRI. Magnetic Resonance in Medicine. 2010
668 apr;63(5):1144-53.
- 669 75 Setsompop K, Gagoski BA, Polimeni JR, Witzel T, Wedeen VJ, Wald LL. Blipped-controlled
670 aliasing in parallel imaging for simultaneous multislice echo planar imaging with reduced g
671 -factor penalty. Magnetic Resonance in Medicine. 2011 aug;67(5):1210-24.
- 672 76 Jenkinson M, Beckmann CF, Behrens TEJ, Woolrich MW, Smith SM. FSL. NeuroImage. 2012
673 aug;62(2):782-90.
- 674 77 Jenkinson M, Smith S. A global optimisation method for robust affine registration of brain
675 images. Medical Image Analysis. 2001 jun;5(2):143-56.
- 676 78 Posse S, Wiese S, Gembris D, Mathiak K, Kessler C, Grosse-Ruyken ML, et al. Enhancement
677 of BOLD-contrast sensitivity by single-shot multi-echo functional MR imaging. Magnetic Res-
678 once in Medicine. 1999 jul;42(1):87-97.
- 679 79 Cox RW. AFNI: Software for Analysis and Visualization of Functional Magnetic Resonance
680 Neuroimages. Computers and Biomedical Research. 1996 jun;29(3):162-73.
- 681 80 Andersson JLR, Skare S, Ashburner J. How to correct susceptibility distortions in spin-echo
682 echo-planar images: application to diffusion tensor imaging. NeuroImage. 2003 oct;20(2):870-
683 88.

- 684 81 Glasser MF, Smith SM, Marcus DS, Andersson JLR, Auerbach EJ, Behrens TEJ, et al. The Human
685 Connectome Project's neuroimaging approach. *Nature Neuroscience*. 2016 aug;19(9):1175-
686 87.
- 687 82 Behzadi Y, Restom K, Liau J, Liu TT. A component based noise correction method (CompCor)
688 for BOLD and perfusion based fMRI. *NeuroImage*. 2007 aug;37(1):90-101.
- 689 83 Patriat R, Molloy EK, Birn RM. Using Edge Voxel Information to Improve Motion Regression
690 for rs-fMRI Connectivity Studies. *Brain Connectivity*. 2015 nov;5(9):582-95.
- 691 84 Tagliazucchi E, Balenzuela P, Fraiman D, Chialvo DR. Criticality in large-scale brain fMRI
692 dynamics unveiled by a novel point process analysis. *Frontiers in physiology*. 2012;3:15.
- 693 85 Liu X, Zhang N, Chang C, Duyn JH. Co-activation patterns in resting-state fMRI signals.
694 *NeuroImage*. 2018 oct;180:485-94.
- 695 86 Raguet H, Fadili J, Peyré G. A Generalized Forward-Backward Splitting. *SIAM Journal on
696 Imaging Sciences*. 2013 jan;6(3):1199-226.
- 697 87 Friedrich J, Zhou P, Paninski L. Fast online deconvolution of calcium imaging data. *PLOS
698 Computational Biology*. 2017 mar;13(3):e1005423.
- 699 88 Jewell SW, Hocking TD, Fearnhead P, Witten DM. Fast nonconvex deconvolution of calcium
700 imaging data. *Biostatistics*. 2019 feb;21(4):709-26.
- 701 89 Farouj Y, Karahanoglu FI, Van De Ville D. Deconvolution of Sustained Neural Activity
702 From Large-Scale Calcium Imaging Data. *IEEE Transactions on Medical Imaging*. 2020
703 apr;39(4):1094-103.
- 704 90 Lindquist MA, Waugh C, Wager TD. Modeling state-related fMRI activity using change-point
705 theory. *NeuroImage*. 2007 apr;35(3):1125-41.
- 706 91 Liu X, Duyn JH. Time-varying functional network information extracted from brief
707 instances of spontaneous brain activity. *Proceedings of the National Academy of Sciences*. 2013
708 feb;110(11):4392-7.
- 709 92 Liu X, Chang C, Duyn JH. Decomposition of spontaneous brain activity into distinct fMRI
710 co-activation patterns. *Frontiers in Systems Neuroscience*. 2013;7:101.
- 711 93 Cifre I, Flores MTM, Ochab JK, Chialvo DR. Revisiting non-linear functional brain co-
712 activations: directed, dynamic and delayed; 2020.
- 713 94 Cifre I, Zarepour M, Horovitz SG, Cannas SA, Chialvo DR. Further results on why a point
714 process is effective for estimating correlation between brain regions. *Papers in Physics*. 2020
715 jun;12:120003.
- 716 95 Zhang X, Pan WJ, Keilholz SD. The relationship between BOLD and neural activity arises
717 from temporally sparse events. *NeuroImage*. 2020 feb;207:116390.
- 718 96 Tagliazucchi E, Balenzuela P, Fraiman D, Montoya P, Chialvo DR. Spontaneous BOLD event
719 triggered averages for estimating functional connectivity at resting state. *Neuroscience letters*.
720 2011 Jan;488:158-63.

- 721 97 Tagliazucchi E, Siniatchkin M, Laufs H, Chialvo DR. The Voxel-Wise Functional Connectome
722 Can Be Efficiently Derived from Co-activations in a Sparse Spatio-Temporal Point-Process.
723 Frontiers in neuroscience. 2016;10:381.
- 724 98 Rolls ET, Cheng W, Feng J. Brain dynamics: Synchronous peaks, functional connectivity, and
725 its temporal variability. Human brain mapping. 2021 Jun;42:2790-801.
- 726 99 Deco G, Kringelbach ML. Hierarchy of Information Processing in the Brain: A Novel 'Intrinsic
727 Ignition' Framework. Neuron. 2017 Jun;94:961-8.
- 728 100 Deco G, Tagliazucchi E, Laufs H, Sanjuán A, Kringelbach ML. Novel Intrinsic Ignition Method
729 Measuring Local-Global Integration Characterizes Wakefulness and Deep Sleep. eNeuro.
730 2017;4.
- 731 101 Faskowitz J, Esfahlani FZ, Jo Y, Sporns O, Betzel RF. Edge-centric functional network rep-
732 resentations of human cerebral cortex reveal overlapping system-level architecture. Nature
733 neuroscience. 2020 Dec;23:1644-54.
- 734 102 Esfahlani FZ, Jo Y, Faskowitz J, Byrge L, Kennedy DP, Sporns O, et al. High-amplitude
735 cofluctuations in cortical activity drive functional connectivity. Proceedings of the National
736 Academy of Sciences. 2020 oct;117(45):28393-401.
- 737 103 Jo Y, Faskowitz J, Esfahlani FZ, Sporns O, Betzel RF. Subject identification using edge-centric
738 functional connectivity. NeuroImage. 2021 Jun;238:118204.
- 739 104 Sporns O, Faskowitz J, Teixeira AS, Cutts SA, Betzel RF. Dynamic expression of brain
740 functional systems disclosed by fine-scale analysis of edge time series. Network neuroscience
741 (Cambridge, Mass). 2021;5:405-33.
- 742 105 van Oort ESB, Mennes M, Navarro Schröder T, Kumar VJ, Zaragoza Jimenez NI, Grodd W,
743 et al. Functional parcellation using time courses of instantaneous connectivity. NeuroImage.
744 2018 Apr;170:31-40.
- 745 106 Yeşilyurt B, Uğurbil K, Uludağ K. Dynamics and nonlinearities of the BOLD response at very
746 short stimulus durations. Magnetic resonance imaging. 2008 Sep;26:853-62.
- 747 107 Sadaghiani S, Uğurbil K, Uludağ K. Neural activity-induced modulation of BOLD poststimulus
748 undershoot independent of the positive signal. Magnetic resonance imaging. 2009 Oct;27:1030-
749 8.
- 750 108 Chen JE, Glover GH, Fultz NE, Rosen BR, Polimeni JR, Lewis LD. Investigating mechanisms
751 of fast BOLD responses: The effects of stimulus intensity and of spatial heterogeneity of
752 hemodynamics. NeuroImage. 2021 dec;245:118658.
- 753 109 Polimeni JR, Lewis LD. Imaging faster neural dynamics with fast fMRI: A need for updated
754 models of the hemodynamic response. Progress in neurobiology. 2021 Dec;207:102174.
- 755 110 Gonzalez-Castillo J, Saad ZS, Handwerker DA, Inati SJ, Brenowitz N, Bandettini PA. Whole-
756 brain, time-locked activation with simple tasks revealed using massive averaging and model-free
757 analysis. Proceedings of the National Academy of Sciences of the United States of America.
758 2012 Apr;109:5487-92.

- 759 111 Farouj Y, Karahanoglu FI, Van De Ville D. Bold Signal Deconvolution Under Uncertain
760 HÆModynamics: A Semi-Blind Approach. In: 2019 IEEE 16th International Symposium on
761 Biomedical Imaging (ISBI 2019). IEEE; 2019. p. 1792-6.
- 762 112 Cherkaoui H, Moreau T, Halimi A, Leroy C, Ciuciu P. Multivariate semi-blind deconvolution
763 of fMRI time series. NeuroImage. 2021 nov;241:118418.
- 764 113 Uruñuela-Tremiño E, Moia S, Gonzalez-Castillo J, Caballero-Gaudes C. Deconvolution of
765 multi-echo functional MRI data with Multivariate Multi-Echo Sparse Paradigm Free Mapping.
766 ISMRM 27th Annual Meeting and Exhibition. 2019 May.
- 767 114 Uruñuela E, Moia S, Caballero-Gaudes C. A Low Rank and Sparse Paradigm Free Mapping
768 Algorithm For Deconvolution of fMRI Data. In: 2021 IEEE 18th International Symposium on
769 Biomedical Imaging (ISBI). IEEE; 2021. .
- 770 115 Meinshausen N, Bühlmann P. Stability selection. Journal of the Royal Statistical Society:
771 Series B (Statistical Methodology). 2010 jul;72(4):417-73.
- 772 116 Akçakaya M, Yaman B, Chung H, Ye JC. Unsupervised Deep Learning Methods for Biological
773 Image Reconstruction. arXiv. 2021 May.
- 774 117 Monga V, Li Y, Eldar YC. Algorithm Unrolling: Interpretable, Efficient Deep Learning for
775 Signal and Image Processing. IEEE Signal Processing Magazine. 2021;38(2):18-44.
- 776 118 Ongie G, Jalal A, Metzler CA, Baraniuk RG, Dimakis AG, Willett R. Deep Learning Tech-
777 niques for Inverse Problems in Imaging. IEEE Journal on Selected Areas in Information Theory.
778 2020;1(1):39-56.
- 779 119 Cherkaoui H, Sulam J, Moreau T. Learning to solve TV regularised problems with unrolled
780 algorithms. Advances in Neural Information Processing Systems. 2020;33:11513-24.

781 Supplementary Material for Hemodynamic Deconvolution Demystified: 782 Sparsity-Driven Regularization at Work

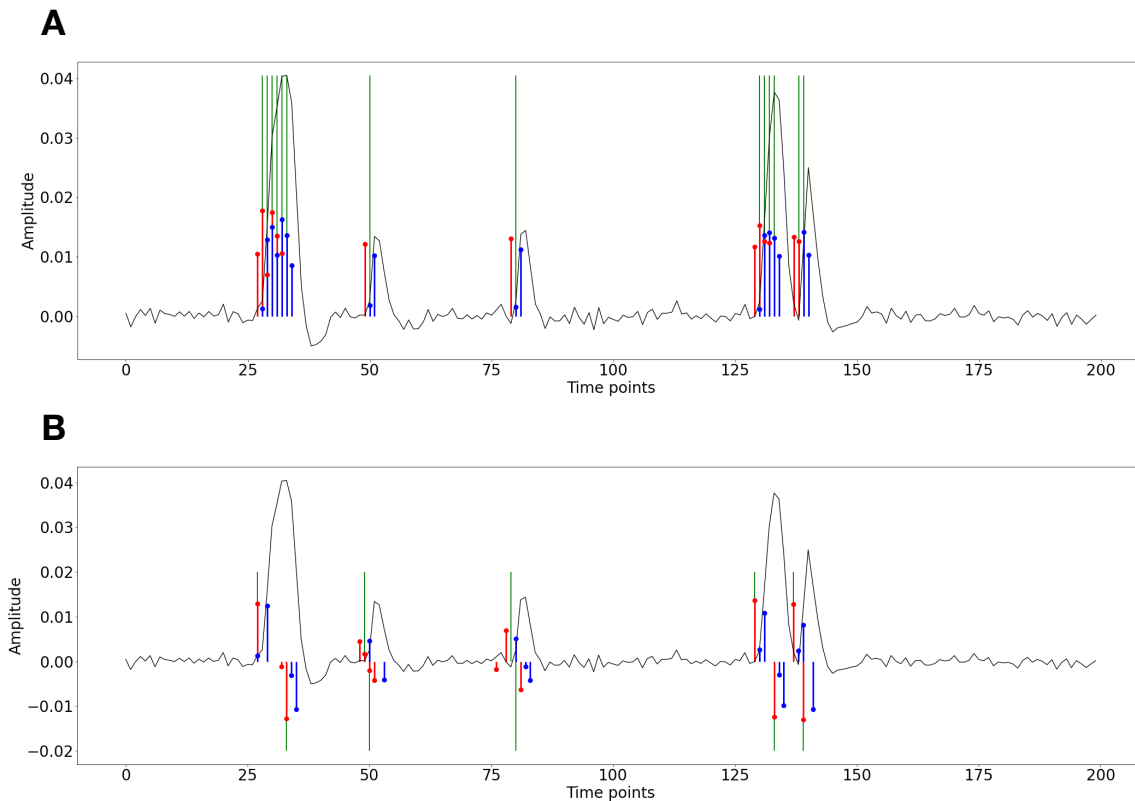


Figure S1: Activity-inducing (A) and innovation (B) signals estimated with PFM (red) and TA (blue) using their built-in HRF as opposed to using the same. The black line depicts the simulated signal, while the green lines indicate the onsets of the simulated neuronal events. X axis shows time in TRs.

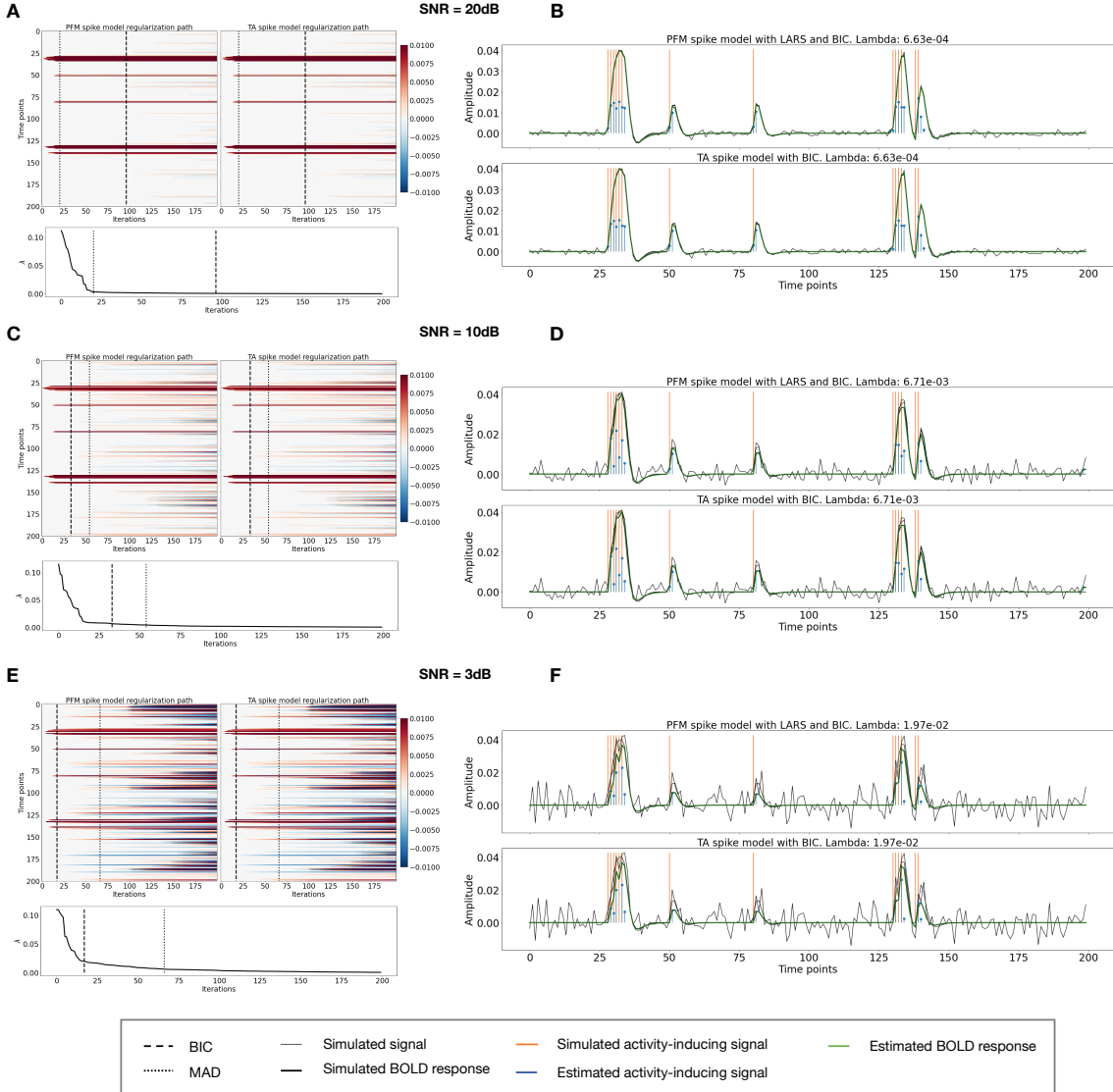


Figure S2: Spike model simulations. (Left) Heatmap of the regularization paths of the activity-inducing signal estimated with PFM and TA as a function of λ (increasing number of iterations in x-axis), whereas each row in the y-axis shows one time-point. Vertical lines denote iterations corresponding to the Akaike and Bayesian Information Criteria (AIC and BIC) optima. (Right) Estimated activity-inducing (blue) and activity-related (green) signals when set based on BIC. All estimates are identical, regardless of SNR.

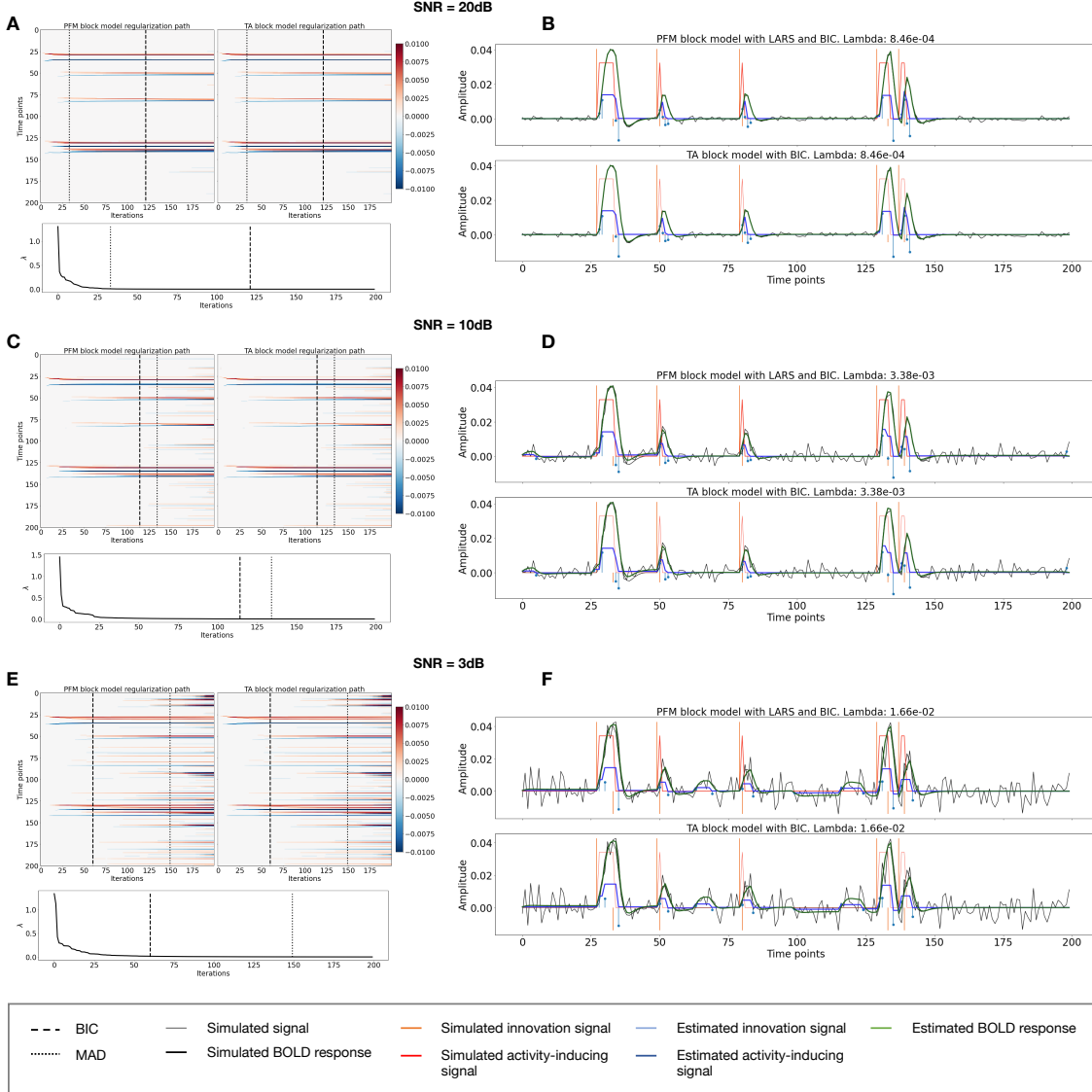


Figure S3: Block model simulations. (Left) Heatmap of the regularization paths of the innovation signal estimated with PFM and TA as a function of λ (increasing number of iterations in x-axis), whereas each row in the y-axis illustrates one time-point. Vertical lines denote iterations corresponding to the Akaike and Bayesian Information Criteria (AIC and BIC) optima. (Right) Estimated innovation (blue) and activity-related (green) signals when λ is set based on BIC. All the estimates are identical when compared between the PFM and TA cases, regardless of SNR.

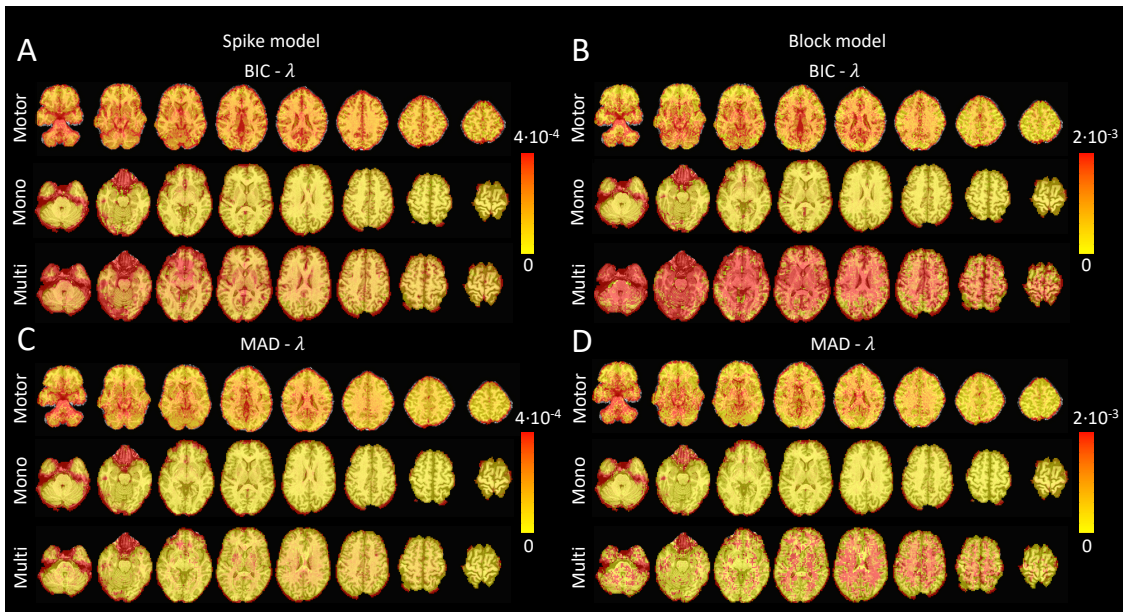


Figure S4: Values of λ across the different voxels in the brain used to estimate (A) the activity-inducing signal (spike model) and (B) the innovation signal (block model) with the BIC selection, as well as (C) the activity-inducing signal (block model) and (D) the innovation signal (block model) with a MAD-based selection. The λ maps are shown for the three experimental fMRI datasets: the motor task (Motor), the monoband resting-state (Mono), and the multiband resting-state (Multi) datasets.

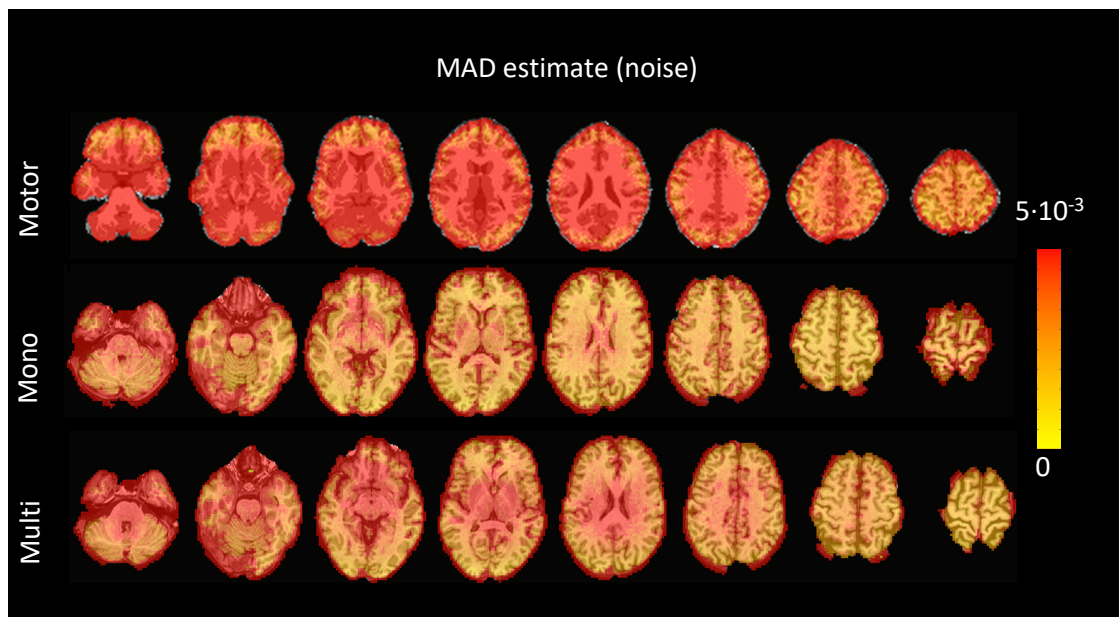


Figure S5: Values of the MAD estimate of standard deviation of the noise across the different voxels in the brain for the three experimental fMRI datasets: the motor task (Motor), the monoband resting-state (Mono), and the multiband resting-state (Multi) datasets.

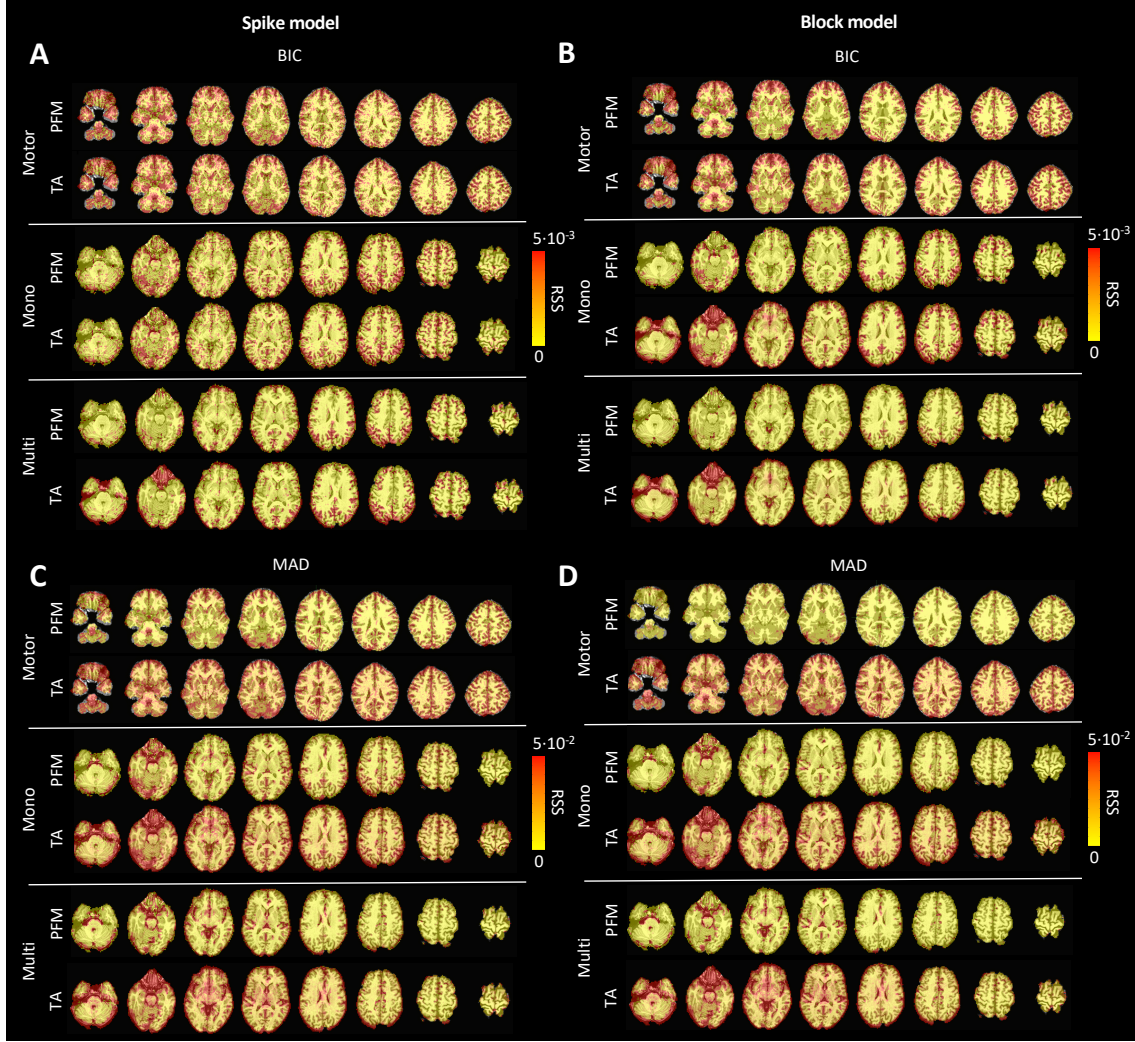


Figure S6: Root sum of squares (RSS) comparison between Paradigm Free Mapping and Total Activation for the three experimental fMRI datasets: the motor task (Motor), the monoband resting-state (Mono), and the multiband resting-state (Multi) datasets. RSS maps are shown for the spike (left) and block (right) models solved with a selection of λ based on the BIC (top) and MAD (bottom) criteria.

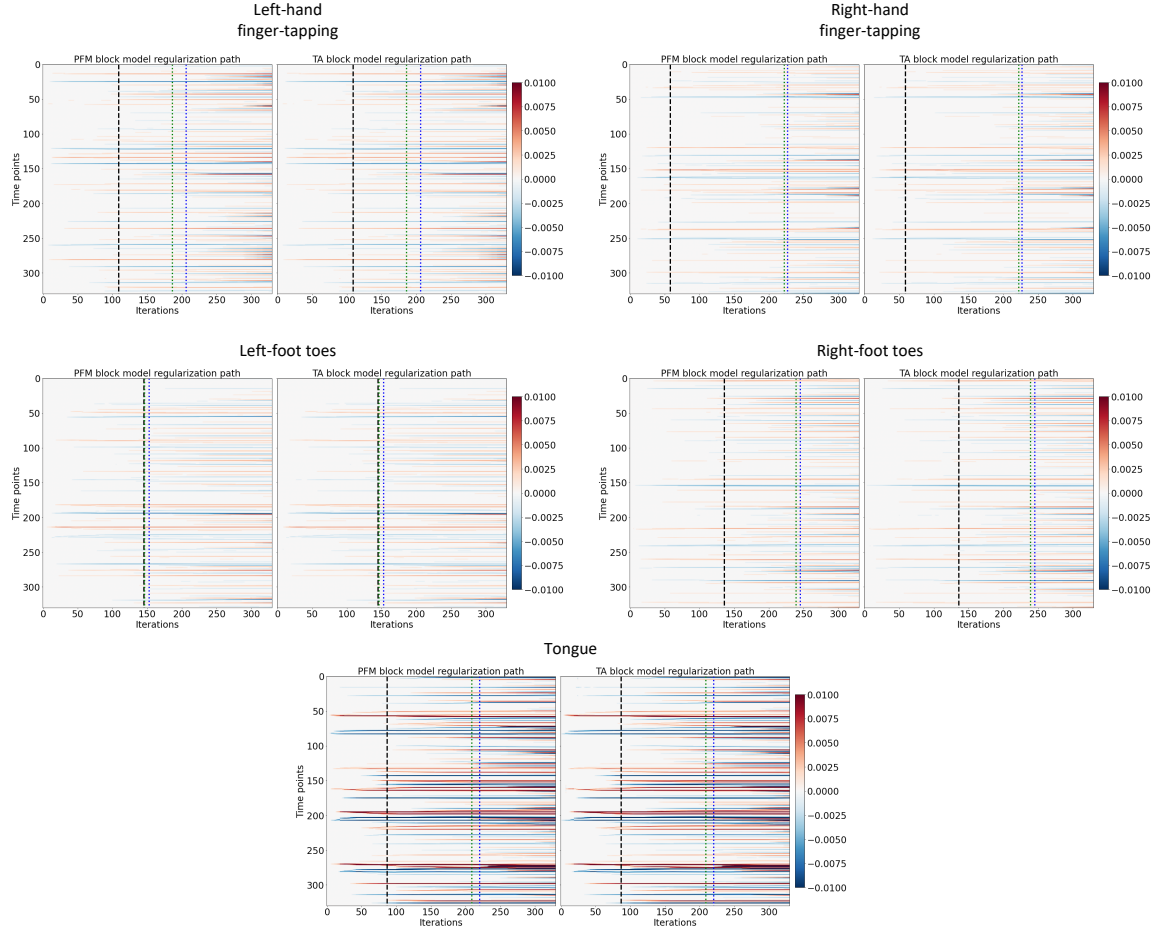


Figure S7: Regularization paths of the innovation signal estimated with PFM and TA as a function of λ (increasing number of iterations in x-axis, whereas each row in the y-axis shows one time-point) for the representative voxels of the motor task shown in Figure 5. Vertical lines denote selections of λ corresponding to the BIC (black), MAD based on LARS residuals (blue) and MAD based on FISTA residuals (green) optima.

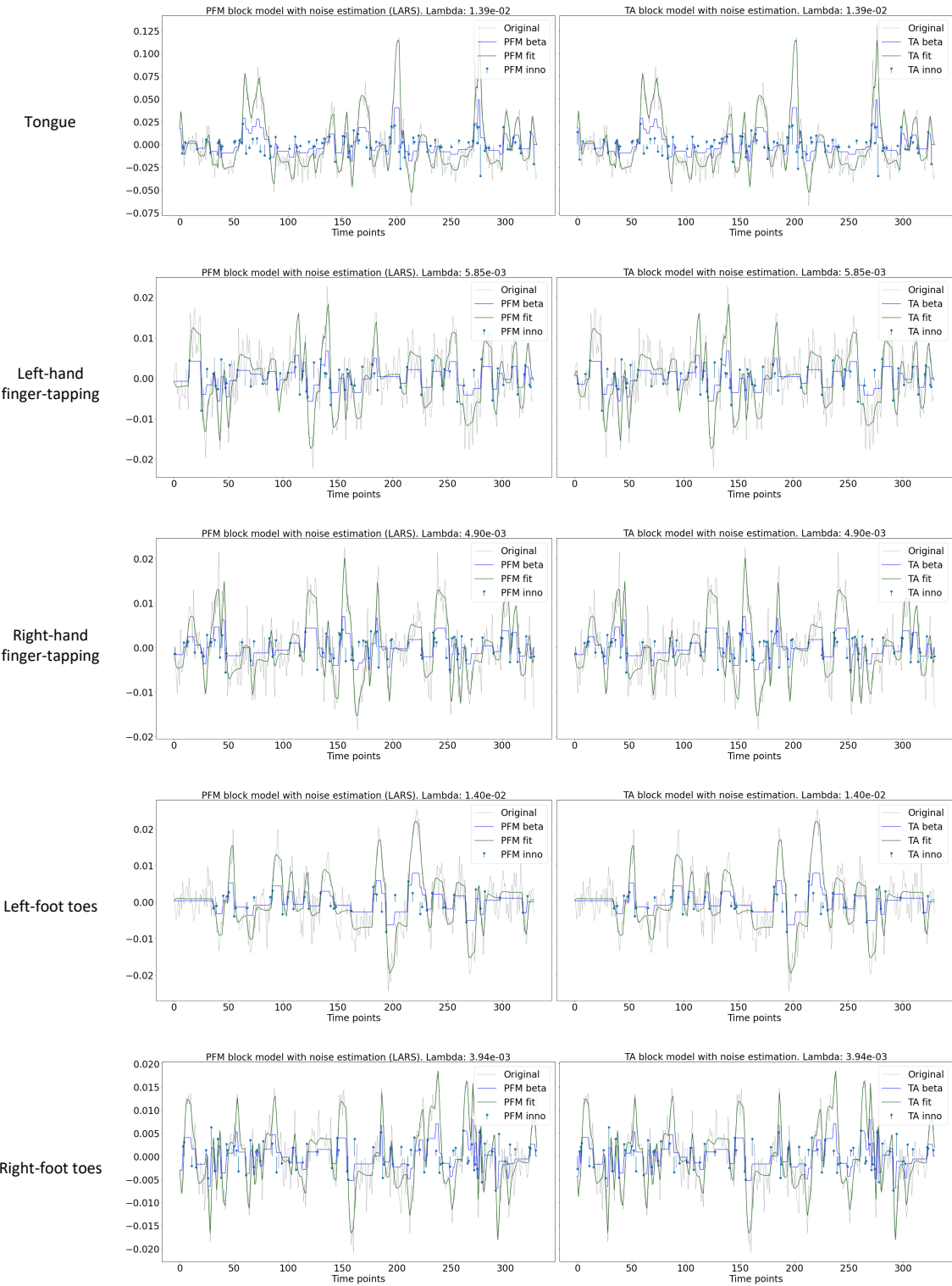


Figure S8: Estimated innovation signal (blue) and activity-related signal (green) for the representative voxels of the motor task shown in Figure 5 with the MAD selection of λ made by TA, i.e., employing the same λ with both PFM and TA.

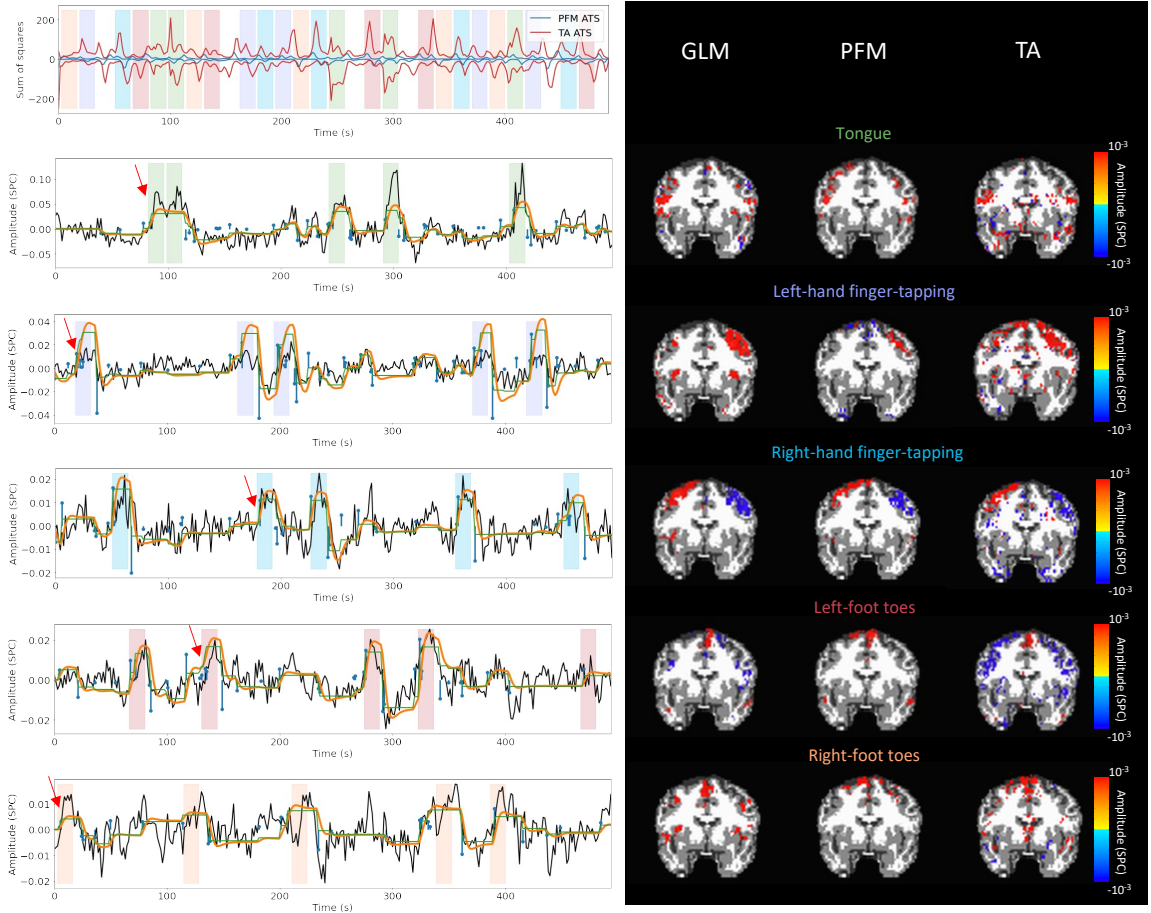


Figure S9: Activity maps of the motor task using a selection of λ based on the MAD estimate. Row 1: Activation time-series of the innovation signals estimated by PFM (in blue) or TA (in red) calculated as the sum of squares of all voxels at every timepoint. Positive-valued and negative-valued contributions were separated into two distinct timecourses. Color-bands indicate the onset and duration of each condition in the task (green: tongue, purple: left-hand finger-tapping, blue: right-hand finger-tapping, red: left-foot toes, orange: right-foot toes). Rows 2-6: time-series of a representative voxel for each task with the PFM-estimated innovation (blue), PFM-estimated activity-inducing (green), and activity-related (i.e., fitted, orange) signals, with their corresponding GLM, PFM, and TA maps on the right. The maps shown on the right are sampled at the time-point labeled with the red arrows and display the innovation signals at that moment across the whole brain.

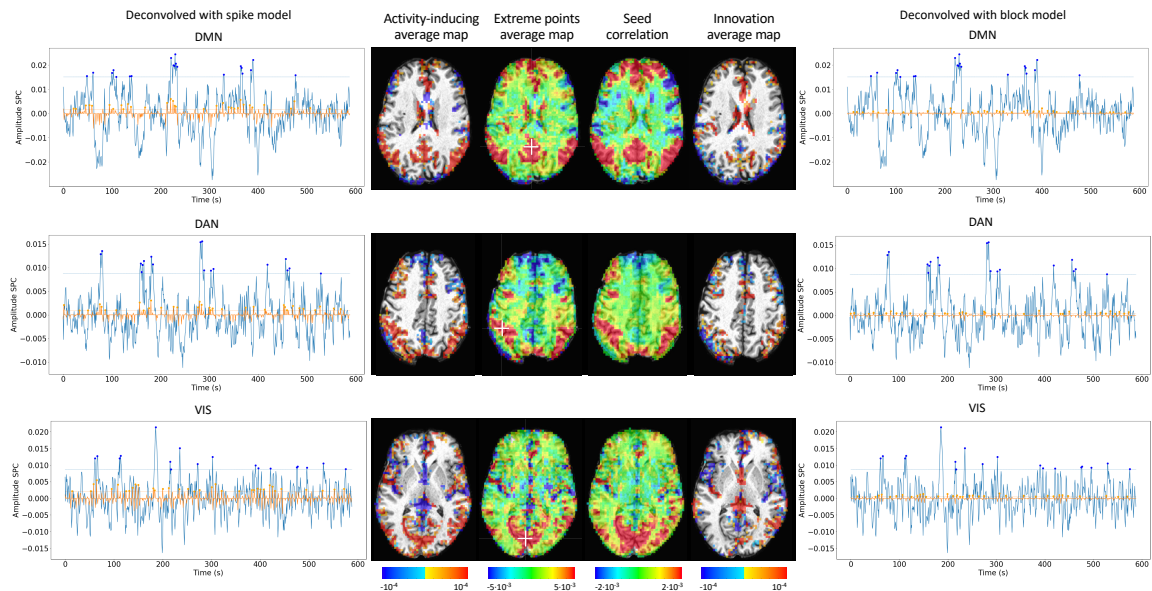


Figure S10: Activity-inducing CAPs (left) and innovation CAPs (right) obtained with the PFM-estimated activity-inducing and innovation signals respectively, using a MAD-based selection of λ . Time-points selected with a 95th percentile threshold are shown over the average time-series (blue) in the seed region (white-cross) and the deconvolved signal (orange). CAPs and seed correlation maps are illustrated in the center.